

Electronic Thesis and Dissertation Repository

8-24-2021 10:30 AM

A quantitative assessment of hemodynamic and histological parameters in the mdx mouse model

Sarah Hakim, *The University of Western Ontario*

Supervisor: Hoffman, Lisa M., *The University of Western Ontario*

A thesis submitted in partial fulfillment of the requirements for the Master of Science degree in Medical Biophysics

© Sarah Hakim 2021

Follow this and additional works at: <https://ir.lib.uwo.ca/etd>



Part of the [Biophysics Commons](#)

Recommended Citation

Hakim, Sarah, "A quantitative assessment of hemodynamic and histological parameters in the mdx mouse model" (2021). *Electronic Thesis and Dissertation Repository*. 8240.

<https://ir.lib.uwo.ca/etd/8240>

This Dissertation/Thesis is brought to you for free and open access by Scholarship@Western. It has been accepted for inclusion in Electronic Thesis and Dissertation Repository by an authorized administrator of Scholarship@Western. For more information, please contact wlsadmin@uwo.ca.

Abstract

Duchenne muscular dystrophy (DMD) is one of the most commonly inherited musculoskeletal disorders affecting 1 in 3500 boys worldwide. The disorder is due to a lack of functional dystrophin protein, which, in turn, results in a loss of cell membrane integrity in skeletal, cardiac muscle and the brain leading to changes in perfusion. As such, within DMD tissue, necrosis is commonly observed, and it has been previously hypothesized that this may be due to a reduction in regional blood supply. Here, we aim to measure hemodynamic changes during disease progression in DMD (*Mdx/Utrn*^{+/+}) mice, using dynamic contrast enhanced computed tomography imaging and histology across two time points; 4-5 weeks and 8-10 weeks.

Preliminary DCE-CT data collected at the 4–5-week time point (n=3-5) showed a 17.00% increase in blood flow (p=0.14) and 16.06% (p=0.13) increase in blood volume in the brain between *Mdx/Utrn*^{+/+} and *C57bl/10 mice*. Similarly, the heart showed an increase in blood flow by 8.76% (p=0.29) and increased blood volume by 9.47% (p=0.22) between the two groups at the same time point. Furthermore, pathologic differences in (*Mdx/Utrn*^{+/+}) mice have been shown within the cardiac, brain, and skeletal muscle tissue compared to the wild-type mice (*C57bl/10*). Currently, there is insufficient knowledge of functional tissue perfusion parameters in DMD. Therefore, this research will provide insight as to whether or not non-invasive diagnostic measures can assess perfusion differences before the onset of serious complications leading to death.

Keywords: Duchenne muscular dystrophy, Ischemia, CT perfusion, Oxidative Stress, *Mdx*

Summary for Lay Audience

Duchenne muscular dystrophy (DMD) is one of the most commonly inherited musculoskeletal disorders affecting 1 in 3500 boys. The disorder is due to a lack of functional dystrophin protein, which, in turn, results in a loss of cell membrane integrity in skeletal, cardiac muscle and the brain leading to changes in perfusion. As such, within DMD tissue, necrosis is commonly observed, and it has been previously hypothesized that this may be due to a reduction in regional blood supply. Here, we aim to measure hemodynamic changes during disease progression in the *Mdx/Utrn*^{+/+} murine model of DMD and *C57bl/10* mice using dynamic contrast enhanced computed tomography (DCE-CT) imaging across two time points; 4-5 weeks and 8-10 weeks. These time points have been associated with the pre-fibrotic condition and onset of fibrosis respectively within literature.

Furthermore, pathologic differences in (*Mdx/Utrn*^{+/+}) mice have been shown within the cardiac, brain, and skeletal muscle tissue compared to the wild-type mice (*C57bl/10*) and were used to validate DCE-CT data. Currently, there is insufficient knowledge of functional tissue perfusion parameters in DMD. Therefore, this research may provide guidance as to whether or not it is feasible that non-invasive diagnostic measures can assess perfusion differences before the onset of complications.

Acknowledgments

Firstly, I would like to thank my supervisor, Dr. Lisa Hoffman, for her encouragement and guidance throughout my time in her lab. Your positive attitude is infectious and has inspired me for these past four years. Thank you for taking me on as a volunteer, work-study student, summer student, and eventual graduate student.

I would like to thank my advisory committee members, Drs. Aaron So and Krishna Singh for their continuous support and constructive feedback. Their mentorship helped navigate the direction of my research during challenging times.

In addition, I would like to extend a huge thank you to members of the Lee lab. Especially Jennifer Hadway and Lise Desjardins, for all their assistance during my imaging days. Those sessions were highly productive due to your expertise and were filled with many laughs and memories. Thank you to Drs. Ting Lee and Xiaogang Chen for all their guidance and access to the CTP software to generate the perfusion maps. Thank you to Anne Leaist, who helped coordinate my visits to Robarts to access the workstations per local health guidelines.

Thank you to Caroline O'Neil, who performed Masson's Trichrome staining, H&E staining, and the sectioning of paraffin-embedded tissues at Robarts Research Institute. Furthermore, I would like to extend my gratitude to past and present members of the Hoffman lab. They were able to provide me with a skillset to advance my scientific knowledge throughout my time. Finally, I wish to express my sincere gratitude to all my friends at Western, Robarts Research Institute, and Lawson Health Research Institute.

I would like to acknowledge funding support from the CIHR Fredrick Banting and Charles Best Canada Scholarship, Western Graduate Research Scholarship, and Western's Interdisciplinary Development Initiative (IDI) in Stem Cell and Regenerative Medicine studentship. In addition, funding support from Dr. Hoffman's lab stemming from CHRI, and NSERC. Thank you to the Department of Medical Biophysics and the Collaborative Program in Molecular Imaging for their continuous guidance throughout my degree.

Table of Contents

Abstract.....	ii
Summary for Lay Audience.....	iii
Acknowledgments.....	iv
Table of Contents.....	v
List of Figures.....	viii
List of Tables.....	xi
List of Abbreviations.....	xii
List of Appendices.....	xiv
Chapter 1.....	1
1 Introduction.....	1
1.1 Clinical indications of DMD.....	1
1.1.1 Overview.....	1
1.1.2 Diagnosis.....	2
1.2 Pathophysiology.....	5
1.2.1 Skeletal Muscle.....	5
1.2.2 Heart.....	6
1.2.3 Brain.....	8
1.3 Myeloperoxidase.....	9
1.4 Oxidative Stress contributes to Hemodynamics Outcome.....	11
1.5 Measures of Perfusion Parameters.....	13
1.6 Murine Models of DMD.....	15
1.7 Research Outline.....	17
1.7.1 Study Hypothesis.....	17
1.7.2 Study Objectives.....	18

1.8	References.....	19
Chapter 2	28
2	In-vivo whole-body CT perfusion imaging.....	28
2.1	Introduction.....	28
2.2	Materials and Methods.....	30
2.2.1	Study Population.....	30
2.2.2	DCE- CT Imaging Protocol and Analysis Overview.....	31
2.2.3	Histology.....	31
2.2.4	Statistical Analysis.....	33
2.3	Results.....	33
2.3.1	Arterial Enhancement Curves display notable differences between the 4-5 week pre-fibrotic time point and 8-10 week fibrotic time point in DMD	33
2.3.2	Increases in blood flow and blood volume deemed not significant in DMD brain tissue at 4-5 weeks of age	35
2.3.3	Changes in hemodynamic parameters within the myocardium are deemed not statistically significant at the 4-5 week and 8-10 week time points in DMD	39
2.3.4	Differences in hemodynamic parameters are deemed not statistically significant at both 4-5 week and 8-10 week time points in DMD hindlimb regions.....	42
2.3.5	Comparison of blood flow at the 4-5 week and 8-10 week time points ...	45
2.3.6	Comparison of blood volume at the 4-5 week and 8-10 week time points	46
2.3.7	Comparison of mean transit time at the 4-5 week and 8-10 week time points.....	47
2.3.8	<i>Ex-vivo</i> MPO signal is significantly heightened at the pre-fibrotic time point of 4-5 weeks in DMD brain tissue.....	50
2.3.9	MPO Signal is significantly heightened at the fibrotic time point of 8-10 weeks in DMD heart and skeletal tissue	50
2.3.10	<i>Ex-vivo</i> MPO signal is significantly heightened at the fibrotic time point of 8-10 weeks in DMD cardiac tissue	55

2.3.11 <i>Ex-vivo</i> MPO signal is significantly heightened at the fibrotic time point of 8-10 weeks in DMD skeletal muscle tissue	59
2.4 Discussion	62
2.5 Conclusions	68
2.6 References	70
Chapter 3	74
3 Conclusions and Future Directions	74
3.1 Study Summary	74
3.2 Significance	74
3.3 Limitations	75
3.4 Future Directions	76
3.5 Conclusion	77
3.6 References	79
Appendices	80
Curriculum Vitae	81

List of Figures

Figure 2.1 Average arterial enhancement curve of <i>C57bl/10</i> mice (n=4) compared to <i>mdx</i> mice (n=5) at the 4-to-5-week time point	34
Figure 2.2 Average arterial enhancement curve of <i>C57bl/10</i> mice (n=3) compared to <i>mdx</i> mice (n=3) at the 8-to-10-week time point	35
Figure 2.3 Comparison between <i>C57bl/10</i> and <i>mdx</i> brain regions with respect to blood flow (ml/min/100g), blood volume (ml/100g), and mean transit time (s) at the 4-5 week time point (n=1 biological and n=1 technical replicate per genotype group).	37
Figure 2.4 Comparison between <i>C57bl/10</i> and <i>mdx</i> brain regions with respect to blood flow (ml/min/100g), blood volume (ml/100g), and mean transit time (s) at the 8-10 week time point (n=1 biological and n=1 technical replicate per genotype group).	38
Figure 2.5 Comparison between <i>C57bl/10</i> and <i>mdx</i> myocardium regions with respect to blood flow (ml/min/100g), blood volume (ml/100g), and mean transit time (s) at the 4-5 week time point (n=1 biological and n=1 technical replicate per genotype group).	40
Figure 2.6 Comparison between <i>C57bl/10</i> and <i>mdx</i> cardiac regions with respect to blood flow (ml/min/100g), blood volume (ml/100g), and mean transit time (s) at the 8-10 week time point (n=1 biological and n=1 technical replicate per genotype group).	41
Figure 2.7 Comparison between <i>C57bl/10</i> and <i>mdx</i> hind limb regions with respect to blood flow (ml/min/100g), blood volume (ml/100g), and mean transit time (s) at the 4-5 week time point (n=1 biological and n=1 technical replicate per genotype group).	43
Figure 2.8 Comparison between <i>C57bl/10</i> and <i>mdx</i> hind limb regions with respect to blood flow (ml/min/100g), blood volume (ml/100g), and mean transit time (s) at the 8-10 week time point (n=1 biological and n=1 technical replicate per genotype group).	44
Figure 2.9 Comparison of blood flow to brain, myocardium and hind limbs at the A) 4-5 week time point between <i>mdx</i> (n=5) and <i>C57bl/10</i> mice (n=4) and B) 8-10 week time point between <i>mdx</i> (n=3) and <i>C57bl/10</i> mice (n=3).	46

Figure 2.10 Comparison of blood volume to brain, myocardium and hind limbs at the A) 4-5 week time point between <i>mdx</i> (n=5) and <i>C57bl/10</i> mice (n=4) and the B) 8-10 week time point between <i>mdx</i> (n=3) and <i>C57bl/10</i> mice (n=3).	47
Figure 2.11 Comparison of mean transit time to brain, myocardium and hind limbs at the A) 4-5 week time point between <i>mdx</i> (n=5) and <i>C57bl/10</i> mice (n=4) and at the B) 8-10 week time point between <i>mdx</i> (n=3) and <i>C57bl/10</i> mice (n=3).	48
Figure 2.12 <i>mdx</i> mice at 4-5 weeks and 8-10 weeks exhibit infiltrate within brain tissue.	51
Figure 2.13 <i>Mdx</i> mice at 8-10 weeks exhibit collagen deposition within brain tissue.	52
Figure 2.14 Comparison of <i>mdx</i> mice to <i>C57bl/10</i> at 4-5 weeks and 8-10 weeks, with respect to MPO deposition in neural tissue, exhibits significantly higher signal in <i>mdx</i> at the 4-5 week time point than 8-10 week time point when compared to the <i>C57bl/10</i> group	53
Figure 2.15 Quantified signal of MPO deposition in <i>mdx</i> mice at 4-5 weeks (p=0.01) and 8-10 weeks (p=0.19) compared to <i>C57bl/10</i> mice within brain tissue.	54
Figure 2.16 <i>Mdx</i> mice at 4-5 weeks and 8-10 weeks exhibit mild cases of centric nuclei within cardiac tissue when compared to <i>C57bl/10</i> mice.	55
Figure 2.17 <i>Mdx</i> mice at 4-5 weeks and 8-10 weeks exhibit collagen deposition within cardiac tissue when compared to <i>C57bl/10</i> mice.	56
Figure 2.18 Comparison of <i>mdx</i> mice to <i>C57bl/10</i> at 4-5 weeks and 8-10 weeks with respect to MPO deposition in cardiac tissue, exhibits significantly higher MPO deposition at both time points in <i>mdx</i> group when compared to <i>C57bl/10</i> group.	57
Figure 2.19 Quantified signal of MPO deposition in <i>mdx</i> mice at 4-5 weeks (p=0.11) and 8-10 weeks (p=0.03) compared to <i>C57bl/10</i> mice exhibited within cardiac tissue.	58
Figure 2.20 <i>Mdx</i> mice at 4-5 weeks and 8-10 weeks exhibit centric nuclei within gastrocnemius muscle when compared to <i>C57bl/10</i> mice.	59
Figure 2.21 <i>Mdx</i> mice at 4-5 weeks and 8-10 weeks exhibit collagen deposition within gastrocnemius muscle when compared to <i>C57bl/10</i> mice.	60

Figure 2.22 Comparison of *mdx* mice to *C57bl/10* at 4-5 weeks and 8-10 weeks with respect to MPO deposition in gastrocnemius tissue, exhibit significantly higher MPO deposition at the 8-10 week time point in *mdx* group when compared to *C57bl/10* group..... 61

Figure 2.23 Quantified signal of MPO deposition in *mdx* mice at 4-5 weeks ($p=0.99$) and 8-10 weeks ($p=0.006$) compared to *C57bl/10* mice within gastrocnemius muscle. 62

List of Tables

Table 1. Quantitative values for Blood flow (ml/min/100g), Blood Volume (ml/100g), and Mean Transit Time (s) at A) the 4-5 week time point and B) 8-10 week time point between <i>C57bl/10</i> and <i>mdx</i> mice.	49
Table 2. Summary of qualitative changes within hemodynamic parameters (blood flow, blood volume, mean transit time) and MPO signal between the 4-5 week and 8-10 week time point.	68

List of Abbreviations

BBB	Blood brain barrier
BF	Blood Flow
BSA	Bovine serum albumin
BV	Blood Volume
<i>C57bl/10</i>	Wild-type
CCAC	Canadian Council on Animal Care
cGMP	Cyclic guanosine monophosphate
CMR	Cardiovascular magnetic resonance imaging
CNS	Central nervous system
DAMP	Damage associated molecular pattern
DAPC	Dystrophin-associated protein complex
DAPI	4',6-diamidino-2-phenylindole
DCE-CT	Dynamic contrast enhanced computed tomography
DCM	Dilated Cardiomyopathy
DKO	Double knock out
DMD	Duchenne Muscular Dystrophy
ECM	Extracellular matrix
EEG	Electroencephalography
fNIRS	Functional near-infrared spectroscopy
GABA	Gamma-aminobutyric acid
GAPDH	Glyceraldehyde 3-phosphate dehydrogenase
GTP	Guanosine triphosphate
H&E	Hematoxylin and Eosin
H₂O₂	Hydrogen peroxide
HMGB1	High mobility group box 1
HOCl	Hypochlorous acid
HU	Hounsfield units
IHC	Immunohistochemistry
iNOS	Inducible nitric oxide synthase
<i>Mdx</i>	Dystrophin null mouse
MHC1	Major histocompatibility complex 1

MHCII	Major histocompatibility complex II
MPO	Myeloperoxidase
MRI	Magnetic Resonance Imaging
MTT	Mean transit time
NOS	Nitric Oxide Synthase
NOX2	NADPH oxidase type 2
PBS	Phosphate buffer saline
PET	Positron emission tomography
PLA2	Phospholipase A2
PMN	Polymorphonuclear leukocytes
ROS	Reactive oxygen species
SOD	Superoxide dismutase
SPECT	Photon emission computed tomography
TLR	Toll like receptor
TTP	Time to peak

List of Appendices

Appendix A: Approval of Animal Protocols.....	80
---	----

Chapter 1

1 Introduction

1.1 Clinical indications of DMD

1.1.1 Overview

Duchenne Muscular dystrophy (DMD) is an X-linked progressive neuromuscular degenerative disorder caused by the absence or dysfunction of dystrophin protein (427 kD).¹ The primary role of dystrophin is to link F-actin to the extracellular matrix (ECM) by associating with the dystrophin-associated protein complex (DAPC) in the sarcolemma.² The loss of the DAPC exacerbates contraction-induced injury within the muscle leading to myonecrosis. This results in decreased sarcolemma integrity, causing an overall increase cell permeability. When this occurs, calcium ions enter at a faster rate causing protein degradation leading to cell death.³ The dystrophin “DMD” gene can form multiple isoforms within muscle and non-muscle tissues due to alternative splicing and several different promoter regions. The gene itself is approximately 2.2 Mb in size and has one of the highest spontaneous mutation frequencies in humans.⁴ Most mutations disrupt the open reading frame of dystrophin, leading to a loss of stability in the protein.⁵

The disorder affects one in every 3,500 male live births and has a prevalence of 4.78 per 100,000 males, and in addition an incidence of 10.71 to 27.78 per 100,000 males worldwide.⁶ Mutations in the DMD gene located on Xp21 account for the manifestation of the DMD phenotype. Around two-thirds of DMD, cases occur *de novo* due to germline mutations, whereas the remaining one-third occur by inheritance from carrier females. DMD primarily affects males; however, female carriers in rare instances may experience mild symptoms.⁷

Dystrophin contains 79 exons, including an actin-binding domain at the N-terminus, 24 spectrin-like repeat units, a cysteine-rich dystroglycan binding site, and a C-terminal domain.⁸ The majority of dystrophin isoforms are derived from independent promoters located in different tissue sites such as the brain, retina, and heart. For example, Dp140 is

present in the brain, kidney, and retina, while Dp116 is expressed in Schwann cells and the spinal cord. Full-length dystrophin, Dp427, is present in skeletal and cardiac muscle. Lastly, Dp71 is expressed in the retina, kidney, liver, lung, brain, and cardiac tissue. Depending on the isoform of dystrophin affected, differing disease pathologies can arise. For instance, the disruption of Dp427 is primarily associated with a decline in muscle function whereas, disruption in shorter isoforms may contribute to non-muscle associated symptoms in DMD such as cognitive defects within the brain.⁹

Treatment for DMD is primarily based on controlling and ameliorating the symptoms that manifest and their respective complications. Clinical trial research has focused on two medications, Deflazacort and Sildenafil. Deflazacort may treat both muscle function loss and dilated cardiomyopathy (DCM), two of the most common causes of death in DMD patients.¹⁰ While Sildenafil is known to reduce fibrosis and muscle weakness as seen in dystrophin null (*mdx*) murine models, more recently it has been shown to alleviate cardiac dysfunction. When nNOS generates NO, the production of cGMP mediates vasodilation, and when this pathway is impaired it can be salvaged by using a phosphodiesterase type 5 inhibitor, such as sildenafil to prevent the degradation of cGMP.^{11,12} Sildenafil works by counteracting the nitric oxide deficiency at the myofiber membrane in order to improve blood flow. As the disease progresses, treatment may consist of assistive devices that may be used at night or during the day to alleviate breathing difficulties such as hypoventilation and sleep apnea, and wheelchairs to assist in movement as hypertrophy and chronic muscle wasting of the limbs lead to limited mobility.¹³

1.1.2 Diagnosis

Generally, there is around a two-and-a-half-year delay prior to DMD diagnosis in the clinic due to a lack of awareness of DMD symptoms by family members or physicians.¹⁴ Degeneration of skeletal muscle tissue occurs in toddlers around two to three years of age, and complete loss of ambulation by adolescence at 12 years of age. The onset of cardiac degeneration, chronic muscle wasting, and respiratory failure, lead to death before 30.¹⁵

One of the first signs noted in clinic is often skeletal muscle decline, which becomes more prominent as toddlers begin to learn how to walk and stand. Other difficulties include standing, running, walking, jumping, which can be observed by Trendelenburg gait, Gower's sign, and fatigue.¹⁶ Clinicians may also observe delayed motor development, progressive muscle weakness, delayed speech/language development, and pseudohypertrophy. Skeletal muscle decline is progressive and continues throughout patients' years.¹⁷ Research has shown that DMD first affects the proximal muscles and later claims the distal limb muscles. Typically, the lower limbs are affected before the upper external muscles. Overall, clinical examination, family history, and genetic testing remain the most direct methods of DMD classification.¹⁵⁻¹⁷ Phases of DMD are often clinically determined by the rate of progression, symptom severity, age of onset, genetic inheritance, and muscle weakness.¹⁸ In clinic, children can be categorically placed into one of three stages depending on their range of mobility: ambulatory stage, early nonambulatory, and late nonambulatory stage. To eliminate the subjective nature of classification, a greater emphasis on non-invasive methods of DMD classification and assessment is imperative to save time and costs.

Currently, when children experience mild motor delays and fall behind their peer group in physical activity or present with difficulty in routine tasks such as climbing stairs, pediatricians will often analyze blood work for creatine kinase. Creatine kinase is a muscle-specific protein that is often elevated in the event of sarcolemma damage.¹⁹ If increased levels exist, the patient is then referred to a neurologist who will run molecular and genetic testing while further analyzing the DNA for mutations. Other additional methods of diagnosis include monitoring of other serum biomarkers within the plasma, such as microRNAs, specifically miR-1, miR-133, and miR-206. miR-1 and miR-133 are typically downregulated in muscular dystrophies like DMD, while miR-206 is found to be upregulated.²⁰

Following these evaluations, DMD diagnosis is often confirmed by the pathologic confirmation of necrotic myofibers, muscle hypertrophy, and fibrosis as excessive deposition of collagen causes scar formation. Most of these findings are derived from the consequence of contraction-induced injury of the sarcolemma since myofibers are

significantly weakened due to mechanical instability, leading to decreased perfusion within certain areas of the body. Currently, the gold standard for diagnosis in DMD are skeletal muscle biopsies which evaluate functional dystrophin quantity are highly invasive, limited in scope for younger individuals.²¹ Repetitive biopsies to monitor therapeutic interventions can further exacerbate muscle tissue damage and are not practical for long-term monitoring. As the disease progresses, repetitive regeneration and degeneration cycles eventually deplete the muscle stem cell pool.²²

Dystrophin within cardiac myocytes serves the same function as in skeletal muscle. The loss of dystrophin reduces contractile function. Pathological alteration of the ventricular myocardium in DMD patients occurs due to atrophy and remodeling. This restructuring may stem from decreased systolic function and cardiomyocyte destruction. Destruction of cardiomyocytes have been shown to occur in conjunction with inflammatory fatty infiltrate and fibrosis. Ventricular wall thinning is common and is often paired with decreased systolic and diastolic function. However, it doesn't always immediately result in the DCM pathology.¹⁷ Myocardial cell death is often imaged using late gadolinium enhancement during cardiovascular magnetic resonance imaging (CMR) scans. Other diagnostic tools used to assess cardiac condition in patients include echocardiography to assess heart structure through ultrasound and electrocardiography.¹⁵ DMD patients within their last years develop a silent form of cardiomyopathy due to lack of physical activity which is often correlated with atrial arrhythmias and sinus tachycardia.²³

Other clinical symptoms DMD patients can exhibit are behavioral and learning disabilities. Recent studies have shown interest in characterizing DMD within the brain, especially with hopes to include it in diagnostic assessment. One study involving males ages 8-18 years found that DMD patients have a smaller grey matter volume and altered white matter volume when compared to age matched controls.²⁴ Expression of dystrophin within the brain occurs in astrocytes, the blood-brain barrier. In DMD, the disruption of the blood-brain barrier (BBB) results in edema and neuronal dysfunction.²⁵ Dystrophin-associated neurodevelopmental syndrome is a term used to describe the clinical psychiatric and neurological impairments associated with DMD. Intellectual impairment has been correlated with mutations occurring in the dystrophin brain-specific isoform and

is not known to be progressive.²⁶ Diagnostic methods such as positron emission tomography (PET) and single-photon emission computed tomography (SPECT) tend to focus on metabolic changes and the overall connectivity of brain networks.²⁷ While methods such as computed tomography and magnetic resonance imaging better capture the prevalent anatomical abnormalities. In addition, cognitive and behavioral studies have shifted to using electroencephalography (EEG) to discern anomalies pertaining to synaptic function due to loss of dystrophin.²⁸ As there is no cure to DMD, the systemic nature of the disease is treated symptomatically depending on the site of organ, muscle, or tissue dysfunction. A thorough understanding of the pathophysiology presented in DMD patients is crucial to guide clinicians in terms of treatment regimens and case management.

1.2 Pathophysiology

1.2.1 Skeletal Muscle

The absence of functional dystrophin within skeletal muscle affects a wide array of pathways pertaining to fibrosis, inflammation, and oxidative stress. While the degeneration of myofibers required for muscle function and maintenance is apparent, a lesser focus of pathologies such as fibrosis have reported in terms of pathophysiology. The generation of excess connective tissue is seen because of prior regeneration and degeneration cycles that deplete the muscle stem cell pool. When these regenerative cycles occur activated macrophages express CD163, and produce anti-inflammatory factors such as interleukin-10 to mitigate inflammation and enhance satellite cell proliferation.⁴⁸ The absence of dystrophin causes myofiber instability and as such sodium and calcium electrolyte influx can occur in excess leading to ATP depletion as the sodium-potassium pump lacks the appropriate chemical and electrical gradients to continuously generate ATP.⁴⁹ With reduced ATP levels, lactic acid build up within skeletal muscle is a common occurrence. At physiological pH lactic acid is usually present as lactate. Lactate is known to control promoter activity of the collagen gene, which in return causes increases in collagen creation and deposition.⁵⁰ In DMD this further exacerbates the infiltrate environment and can lead to downstream effects influencing oxidative stress.⁵¹

Like the heart, mechanical stress within skeletal muscles can align with oxidative stress. ROS have been suspected to contribute mainly to disease pathology in muscular dystrophy. Skeletal muscle contains a large amount of thiol groups associated with troponin, tropomyosin, myosin, and actin. When oxidant species outnumber anti-oxidants, these groups can be altered, influencing redox reactions involved in contraction coupling and creation of cross bridges, thus impairing contraction.⁵² Nitric oxide synthase (NOS), and Phospholipase A2 (PLA2) are responsible for ROS formation. PLA2 has been noted to affect NO localization within the sarcolemma and increases ROS production within mitochondria due to its calcium-dependent and calcium independent pathways.⁵⁴ Furthermore, within skeletal muscle certain groups of anti-oxidant enzymes have been shown to be upregulated such as superoxide dismutase (SOD), catalase, glutathione reductase, and 8-hydroxy-2'-deoxyguanosine in DMD subjects.⁵⁵ While the characterization of dystrophin and the pathologies arising from its absence have been thoroughly assessed, the connection between these pathophysiology and clinical outcome remains lesser known.

1.2.2 Heart

The absence of functional dystrophin leads to a variety of different pathophysiological mechanisms, which ultimately lead to myocyte death. Typically, dystrophin within cardiomyocytes combines with costameres and presents as a striated pattern in the sarcolemma. Costameres attach the ECM to the Z-disc of the sarcomere via the DAPC and cytoskeletal γ -actin. Here, dystrophin's N-terminal region connects to γ -actin, and its C-terminus links with transmembrane β -dystroglycan playing a crucial role in sarcolemmal stability. β -dystroglycan then goes on to bind with α -dystroglycan, which binds to the ECM via laminin. Loss of dystrophin results in sarcolemma fragility and unregulated permeability during increased workload on myocytes.²⁹ The unregulated permeability of cardiomyocytes has been demonstrated using Evans Blue dye entry to target compromised locations within the membrane where serum protein influx occurs.³⁰

The leakiness of the membrane causes an imbalance in the ion gradients, and as such, ions like calcium levels increase intracellularly. In addition to calcium influx via leaky membrane, transient receptor potential channels and L-type calcium channels may

mediate excessive calcium entry within dystrophic cardiomyocytes during stretch-simulated cation influx.³¹ Excess calcium levels impair electrical activity and contractile function in the heart leading to mitochondrial dysfunction and overall heart failure which restricts blood flow to the body. Within the mitochondria, oxidative metabolism relies upon the negative inner membrane potential for adenosine triphosphate (ATP) synthesis. When increased loads of calcium enter the cell from the surrounding ECM, the mitochondrial permeability transition pore depolarizes, causing an interruption of ATP synthesis until membrane potential is restored. During this event, the cell triggers apoptosis and depletes ATP levels, and releases reactive oxygen species (ROS) and pro-apoptotic factors from the mitochondria into the cytosol.³² During the depletion of ATP within the heart, stored phosphocreatine are converted to ATP due to the physiological demand for energy. Past studies have shown that in *mdx* tissue the ratio between phosphocreatine and ATP is reduced prior to the onset of cardiac fibrosis.³³

The lack of functional dystrophin is related to increased production of ROS contributing towards the pathogenesis of the disease. Nicotinamide adenine dinucleotide phosphate oxidase 2 (NOX2) is a superoxide generating enzyme which has increased expression within myocytes of *mdx* mice during stretch-induced activity. NOX2 is converted by superoxide dismutase to hydrogen peroxide (H₂O₂) and excessive H₂O₂ can lead to oxidation of other biological molecules such as lipids, nucleic acids leading to decreased cell survival. Further evidence has been gathered to show that NOX2-mediated ROS may further contribute to mitochondrial dysfunction and leakiness within the sarcolemma calcium within *mdx* myocytes.³⁴ Specifically, NOX2-mediated ROS has been shown to impair lysosome formation and autophagy in *mdx* mice.³⁵

Multiple cells within cardiac tissue contribute to the generation of fibrosis, such as fibroblasts, endothelial cells, immune cells, and cardiomyocytes. Mechanical stress coupled with other factors such as inflammation can cause profibrotic cytokines and chemokine secretion. Increased cardiomyocyte death leads to further fibrosis as collagen deposition takes over to fill the vacancy.³⁶ Collagen deposition isn't degraded due to matrix metalloproteinases and tissue inhibitors of metalloproteinases. The abundance of necrosis and cell-stress within cardiomyocytes cause an excess of chemokines, cytokines,

ultimately recruiting neutrophils and macrophages to clear the surrounding infiltration further aggravating the condition.^{37,38}

1.2.3 Brain

The absence of dystrophin isoforms within the brain has been associated with cognitive defects in DMD. Within the brain, Dp71 is abundantly expressed, and mutations within this isoform is responsible for the bulk of neurocognitive symptoms in patients. The role of Dp71 isoforms within the brain are numerous, ranging from structural functions such as synapse organization to deoxyribonucleic acid (DNA) repair, and cell division. The absence of Dp71 in DMD has been associated with increased clustering with Kir4.1 and aquaporin-4 leading to intracranial swelling and edema.³⁹ Intracranial edema may affect the leakiness of the vasculature surrounding blood brain barrier which has been found to exist within DMD patients.⁴⁰ In addition to physical abnormalities, the majority of Dp71 is localized in the hippocampal dentate gyrus, which is associated with memory consolidation; a process in which DMD patients encounter difficulties. Interestingly, Dp140 plays an integral role in the central nervous system (CNS) and is expressed in blood vessels, which makes its role in cognitive impairment in DMD evident. Vascular dementia arising from the reduction of blood flow, can lead to oxygen deprivation and exacerbate conditions associated with cognitive impairment.⁴¹ Further, lack of dystrophin has been localized to cortical, subcortical, hippocampal regions of the brain where neurons and glial cells are primarily affected, and the cerebellum where Purkinje cells are impacted in DMD.⁴² Within these regions Dp427 is crucial, Dp427c has been found in hippocampus and cortex neurons, whereas Dp427p is found in cerebellar Purkinje cells.²⁷ Thus, the role of dystrophin and the lack thereof within these areas affect and contribute to deficits in learning, memory, movement, and balance in the patient population.^{43,44}

It has been previously mentioned that chronic inflammation is a hallmark indication of DMD. Cytokines have been known to have a neuromodulatory role within the CNS. Structures such as neurons, glia, and even endothelial cells secrete cytokines and likewise contain the respective receptors to receive cytokine signals which in turn influence cognitive function. It has been noted that interleukin-1 β , tumor necrosis factor α , and interleukin-6 receptors have been found in the hippocampus and are associated with

memory formation. In healthy subjects cytokines have been known to promote and regulate synaptic plasticity, whereas in unhealthy subjects it may lead to neuronal dysfunction.⁴⁵

In terms of oxidative stress within the brain, decreased levels of nitric oxide (NO) can impact the hippocampal region which is primarily responsible for memory formation and synaptic plasticity by reducing neurogenesis.⁴⁵ As previously stated, the loss of dystrophin can lead to downstream pathologies such as calcium influx due to the increased permeability to the ECM. Decreased membrane stability in the brain was observed in one study using proton-nuclear magnetic resonance where choline-containing compounds were increased, signifying increased membrane turnover and degradation in patients.⁴⁶ Another recent paper found that decreased gamma-aminobutyric acid (GABA) inhibition resulted in changes of metabolic activity in the hippocampus region, and in return was associated with an increase in glutathione levels; a common antioxidant molecule also involved in nutrient metabolism and regulation of cellular events.⁴⁷ Both of these studies covered a broad range of ROS being produced during increased brain activity, and one could speculate that this may, in return, influence inflammatory cytokine levels and overall perfusion parameters within brain tissue. Further classification of the role of inflammation, and oxidative stress markers remains elusive with respect to cognition in DMD.

1.3 Myeloperoxidase

Myeloperoxidase (MPO) is abundantly expressed within the innate immune system and is the most abundant protein in human neutrophils.⁵⁶ It is primarily released by neutrophils during the fusion between lysosomes and phagosomes. Following fusion, superoxide anions produced further dissociate into H_2O_2 . A standard chain reaction that occurs is the coupling of H_2O_2 with hypochlorous acid (HOCl), which assists in destruction of invading pathogens.⁵⁷ However, in certain disease conditions the production of these by-products can exacerbate tissue damage if produced in abundance. Prolonged exposure of HOCl ultimately leads to cell death by a range of pathways such as, direct cell lysis, and mitochondrial dysfunction by means of monocyte and macrophage damage.⁵²

Endothelial cell damage mediated by HOCl can lead to further mitochondrial dysfunction, necrosis, and apoptotic cell death. Indicatively, presence of HOCl is also related to oxidation of thiol groups, such as glyceraldehyde 3-phosphate dehydrogenase (GAPDH), which leads to decreased glycolytic activity and reduced ATP production. The downregulation of thiols can disrupt calcium levels which, as seen in the previous section led to various pathophysiologic affects in DMD.⁵⁶

In addition, MPO can cause further damage to DAPC by damaging ECM proteins.⁵⁸ With the mislocalization of neuronal nitric oxide synthase (nNOS) as a consequence of dystrophin loss, NO production is vastly reduced, leading to downstream effects on vasculature. nNOS produces NO and is crucial for the regulation of blood flow with respect to endothelial function as it effects vascular permeability.⁵⁹ Depletion of NO results in a lack of vasodilation and a general increase in inflammation due to a lack of anti-inflammatory control. Vascular-mediated rescue from endothelial NO can be hindered by alternate pathways by combining with free radicals.⁶⁰ As mentioned prior, MPO is a leukocyte derived enzyme that catalyzes ROS, specifically aromatic substrates, into hypochlorous acid when hydrogen peroxide and chloride ions are present, which in turn, contribute to tissue damage via inflammatory environment. Polymorphonuclear leukocytes (PMN) activates MPO, which subsequently in the presence of H₂O₂, consumes endothelial derived NO.⁶¹ Thus, MPO can create further endothelial disarray by reducing the bioavailability of NO.

NO has a multitude of additional functions within the cell, some roles include glucose uptake, regulation of mechanical stress, and blood flow by increasing cyclic guanosine monophosphate (cGMP) production. Typically, NO will bind to guanylate cyclase which then converts guanosine triphosphate (GTP) to cGMP which goes on to activate protein kinase G which directly causes vasodilation in smooth muscle by being part of a positive feedback loop.⁶⁰ Further, it is hypothesized that cGMP may activate KATP channels, causing a decrease in calcium entry resulting in vasodilation through inhibition of the smooth muscle light chain mitigating damage during times of increased blood flow.⁵⁹ In contrast, during increased levels of MPO, activation of the Rho-kinase signaling pathway can lead to disruption in vasodilation. This occurs by means of vascular cell adhesion

molecules which are indirectly upregulated as a result of MPO induced activation of calpain; calpain downregulates NO leading to impaired vasodilatory mechanisms.⁶²

1.4 Oxidative Stress contributes to Hemodynamics Outcome

Most patients presenting with DMD will develop ischemia within some regions of the body due to the continuous cycles of muscle degeneration. The absence of dystrophin is known to cause a loss of localized nNOS, which forms part of the DAPC.^{60,63} Past studies have shown in healthy murine models that nNOS may be responsible for blood flow regulation via pathways pertaining to alpha-adrenergic receptor activation to shunt the vasoconstrictor response and induce dilation in vasculature.⁶⁰ This mechanism is impaired in those with DMD causing further disease pathogenesis.

In DMD patients, this response is ineffective as vasoconstriction is not blunted during sympathetic activation.⁶³ The central theory of oxidative damage in DMD patients occurs in a two-hit hypothesis, the first being that there are increased levels of ischemia due to an absence of NOS, and the second hit stemming from the DAPC defects.⁶⁴ For instance, one of the proteins impacted as a result is nNOS which produces NO. NO is present in high levels in the brain and skeletal muscle. Furthermore, nitric oxide has roles in modulating contractile force, exercise-induced glucose uptake, and myofiber differentiation pathways thus stressing its importance in the body.⁶⁵ Without functional dystrophin, nNOS localization cannot occur due to the absence of functional domains, causing nNOS to delocalize into the cytosol.

There are three isoforms of NOS, nNOS, endothelial NOS, and inducible nitric oxide synthase (iNOS). These isoforms allow for the conversion of L-arginine to L-citrulline, through heme-containing oxidoreductases which generate NO.⁶⁵ NO has a wide variety of roles, as it is involved in neural transmission, muscle contractile function, calcium release from sarcoplasmic reticulum, glucose metabolism, and immune modulation.⁶⁵

Physiological responses due to NO rely on its ability to activate guanylate cyclase and thus increase production of cGMP. Additional responses that depend on NO include processes such as the activation or inhibition of cytochrome P450, hemoxygenase, and

cytochrome c oxidase. These enzymes are involved in roles pertaining to oxidation of biological molecules, vascular inflammation, and production of ATP respectively.⁶⁶

Previous investigations have shown that nNOS null mice, and *mdx* mice have catastrophic defects pertaining to vascular control within tissue.⁶⁵ One research paper determined that the mechanism of nitric oxide was deemed protective by inducing dilation and combating the alpha-adrenergic vasoconstrictor response during sympathetic activation. When this path is either impaired or absent, the onset of functional muscle ischemia occurs and the onset of muscle necrosis ensues.⁶³ For instance, healthy patients had this mechanistic response present in order to reduce muscle tissue oxygenation when exercising whereas in DMD patients during exercise were recorded to have increased levels of oxygenation in skeletal muscle.⁶⁷ As mentioned before, lactic acid accumulation during exercise will dissociate further into lactate, which has severe effects on collagen gene regulation. Lactate causes an excess buildup of collagen within the ECM leading to fibrosis.⁴⁹

Dystrophin deficient muscle is known to be susceptible to contraction-based injury as mentioned previously. The loss of dystrophin in endothelial cells leads to impaired vasodilation when skeletal muscle tissue experiences an increased metabolic load due to sympathetic activation.⁶⁸ Pathologic validation has confirmed little to no expression of nNOS in the sarcolemma of DMD patients.⁶⁹ DMD mice have exhibited an overall decrease in vascular density which may be due to excessive fibrofatty tissue deposits that impede blood flow perfusion to the tissue. Decreased blood perfusion to tissues can further exacerbate cellular stress as repair mechanisms and exogenous dystrophin delivery may not be delivered to the site of damage.⁶⁹

A typical characteristic of muscular dystrophies includes the finding of necrotic fibers in bundles throughout the tissue. It is postulated that these contiguous myofibers may be supplied by a common arterial blood supply source. Past studies have confirmed that this hypothesis has merit since the research has shown that muscular dystrophy phenotypes can be reproduced by inducing microvascular ischemia and infarction injury.⁶⁹

When contraction-based injury occurs, and contents of the cell leak, the body's immune system is activated. Decline in muscle function is often correlated with muscle pathology. Infants affected by DMD generally do not show symptoms of the disease, until their innate immune system is activated. Major histocompatibility complex I (MHCI), toll-like receptors (TLR) and nuclear factor-kappa signaling are activated shortly following birth. Past investigations have shown that specifically TLR 1-4, TLR 7-9 expression is upregulated in the *mdx* murine model of DMD.⁷⁰ The constant release of cytoplasmic contents into the extracellular space can lead to the activation of chronic inflammation. Chronic inflammation is further exacerbated by the constant regeneration and degeneration cycles that deplete the muscle stem cell pool. In this case, neutrophils invade the myofibers, which are then phagocytosed by macrophages. Due to the absence of dystrophin, membrane integrity is disrupted and TLR ligands are leaked into the extracellular matrix, especially those displaying damage associated molecular patterns (DAMPs). DAMPs will then activate high mobility group box 1 (HMGB1) proteins, ROS, and heat shock proteins to be released.⁷¹ MHCI and major histocompatibility complex II (MHCII) receptors are activated on muscle cells through proinflammatory cytokines, leading to the recruitment of B and T cells. When neutrophils are phagocytosed by macrophages, release of MPO by-products cause ROS stress via HOCl which decrease NO bioavailability. This is important recall since HOCl has been shown to inhibit endothelium dependent relaxation thus impairing vascular flow.⁷²

1.5 Measures of Perfusion Parameters

Given the age of onset and diagnosis, healthcare professionals tend to prefer non-invasive imaging methods when monitoring disease progression. Magnetic resonance imaging (MRI), ultrasound, PET, and dynamic contrast enhanced computed tomography (DCE-CT), are some of the most common non-invasive imaging modalities used to measure tissue perfusion. MRI uses radio waves and strong magnetic fields to reproduce the body's internal anatomy. It is useful when rendering 3-D images of internal structures and does not require radiation. It does so by pulsating radio signals towards the patient's body, when these radio waves interact with hydrogen atoms within specific molecules, reflected signals transmitted back are recorded to form the localized image.⁷³ In perfusion

based MRI, a bolus of gadolinium-based contrast agent is passed through the body and measured using T2 weighted images. The tracking of the paramagnetic contrast agent ultimately leads to a signal intensity time curve which can be used to assess vascular permeability, tissue perfusion, and the extravascular space.⁷⁴ Patients undergoing MRI must report if they have any electronic devices contained within their body. For instance, those with cardiac pacemakers are unable to be scanned, as the magnetic field would damage the device. One of the major disadvantages associated with MRI include the length of examination, as keeping young patients still for long periods of time is difficult.⁷⁵ Therefore, other approaches may be taken by family physician and other health care providers in accordance with the family's finances and patient's emotional comfort.

Ultrasound is able to image perfusion by using traditional Doppler signal. Doppler ultrasound measures the change in frequency of ultrasound waves between sender and recipient signals in moving targets such as blood flow. Although doppler is relatively inexpensive and readily available for serial assessments, it is limited to observing larger vessels with fast flow rates and has limited spatial resolution. These disadvantages limit its use in younger patients as DMD is a systemic disease, and the pathogenesis of the disease has been known to cause vascular dysfunction.⁷⁸

PET scans employ the use of radiotracers in the body, via injection, inhalation, or oral uptake. Over time, the tracer will deposit in areas of high metabolic activity. Tracers such as ¹⁵O-water, ¹³N-ammonia, and ⁸²rubidium are often used to gauge blood flow in terms of diagnosis of disease.⁷⁹ While, PET scans may be able to provide a quantitative assessment in terms of blood flow, only a handful of clinics have access to such radiotracers with experienced radiologists to conduct testing and interpret results. Furthermore, the half-life of these radiotracers requires the cyclotron facility to manufacture them on site; such facilities are limited around the world.⁸⁰ Thus, healthcare providers often refer patients for diagnosis and clinical assessment using other imaging modalities and techniques.

DCE-CT perfusion imaging depends on baseline images being acquired without contrast enhancement which is then followed by images taken as an intravenous bolus of contrast

agent is injected. As the contrast agent moves through the vasculature, tissues can be perfused, X-ray signals attenuated and later analyzed using software to generate a time enhancement curve. During the first phase of imaging the contrast agent is primarily located in intravascular locations whereas during the second phase the contrast agent diffuses into the extravascular space allowing for vascular permeability to be calculated. Common parameters used to describe hemodynamic perfusion within tissue include mean transit time, blood flow, and blood volume. The primary advantage of DCE-CT is the direct linear relationship between contrast agent concentration and X-ray attenuation.⁸¹ In addition, DCE-CT is relatively cheap, and widely available. One limitation for DCE-CT includes the using low dose ionizing radiation depending on the anatomy being scanned, however many physicians agree that the risk of adverse effects of radiation are minimal compared to the benefits in terms of disease monitoring and diagnosis.⁸¹ Parents and younger patients are more compliant with this modality as exams require little scan time and have a low cost burden. More recently, family members and healthcare providers have looked towards using DCE-CT to monitor disease progression, and accurate diagnosis in other conditions such as renal cancer; however, there haven't been many studies conducted pertaining to DMD.

1.6 Murine Models of DMD

Three types of DMD phenotype exist within the murine classification: *mdx*, *mdx/utrn*^{+/-}, and *mdx/utrn*^{-/-}. These respectively pertain to the mild, intermediate, and severe phenotypes seen in the DMD clinical population. These models have been created by the ablation of utrophin, an autosomally-encoded dystrophin homologue.⁸²

The homologue protein of dystrophin, utrophin is thought to compensate for the lack of functional dystrophin in mice. It has been shown that when loss of dystrophin occurs, utrophin expression is generally upregulated. Utrophin is structurally similar to dystrophin and can act similarly in function. When comparing the two proteins, utrophin lacks the nNOS-binding site, and two spectrin-like repeats.⁸³ Thus, it isn't able to completely ameliorate the DMD pathology that arises overtime with respect to oxidative stress. Utrophin expression in DMD patients has been known to increase with age and has a positive correlation with increasing disease progression. It has been reported that

dystrophin and utrophin proteins are regulated and expressed in a reciprocal manner. Typically due to the role of dystrophin it is found in the sarcolemma, and utrophin is found in the neuromuscular junction. It is usually only during disease states whereby utrophin expression can occur in the sarcolemma to compensate for the lack of dystrophin⁸⁴

Mdx/utrn^{-/-} mice produced by breeding utrophin null mice with *mdx* mice lack both utrophin and dystrophin expression, resulting in the most severe phenotype of DMD. However, this *mdx/utrn*^{-/-} model is not indicative of the human population, where both dystrophin and utrophin are expressed at varying levels systemically.⁵ The dystrophin and utrophin knockout mice (*mdx/utrn*^{-/-}) are known to commonly present weight loss, scoliosis, joint contractures, retardation and even premature death. Studies conducted with *mdx/utrn*^{-/-} mice are difficult due to the lifespan of 15-20 weeks. Moreover, *mdx/utrn*^{-/-} are less commonly used, as the effect of utrophin cannot be completely discounted in the human population and may play tangential roles in oxidative stress pathways and manifest disorders similar to DMD if deficient.⁸⁵

As a result, the *mdx/utrn*^{+/-} model was developed to provide a compromise between the *mdx* and *mdx/utrn*^{-/-} models. These mice are heterozygous for the utrophin allele and exhibit a slightly more severe phenotype than the *mdx* model but not as severe as *mdx/utrn*^{-/-} model. The use of this phenotype is lesser studied in terms of novel research as results are hard to replicate and validate without the guidance of past literature. Thus, the *mdx* mouse model is often used as a “starter model” when researching unknown links in novel pathways within DMD.⁸⁶

Within the *mdx* murine model, a mutation in exon 23 leads to a premature stop causing the absence of dystrophin. While the expression of dystrophin is impaired, it is important to note that utrophin is an autosomal homologue of dystrophin and can, in part, compensate for the lack of dystrophin in murine models. Past research has extensively characterized the *mdx* mouse model despite observations detailing its milder phenotype when compared to the human population.⁸⁷ Regardless of this limitation, the *mdx* mouse remains a gold standard in DMD research and is the model of choice when conducting

novel research in order to validate data. Research using these mice cautions against usage in the aged *mdx* population, at 40+ weeks, as some symptoms do not manifest along similar timelines as seen in the DMD human population. For instance, these mice do not exhibit severe DCM until much later in life and have a longer lifespan when compared to the aforementioned murine models.⁸⁸

Necrotic fibers are most pronounced between 2-8 weeks of age in *mdx* mice, which is later confirmed by creatine kinase plasma levels. Histologically, necrotic fibers present in a scattered pattern with myopathic grouping. The rapid rate of degeneration and regeneration cycles of myofibers peaks between 3-4 weeks. Further, inflammation within skeletal muscle occurs during 3 weeks of age and reaches maximum amount between 8-16 weeks in this model.⁸⁹ In older *mdx* animal models, unique findings include the fact that gastrocnemius muscle and the diaphragm are severely affected whereas the tibialis anterior is subjected to a higher risk of contraction-induced injury.⁹⁰ A notable finding, which needs to be considered during result interpretation of novel studies. In addition, it has been previously shown that moderate exercise can lead to an escalation in disease course. This is important because the use of exercise in *mdx* mice has been shown to upregulate utrophin.⁸⁵ Thus, the link between utrophin and its effects within pathways pertaining to oxidative stress is unknown. In addition, these observations may explain why current therapeutics and treatments have variable efficacy when translated into the human DMD patient population during clinical trials, since the type of murine model may impact pre-clinical research.

1.7 Research Outline

1.7.1 Study Hypothesis

The intersection of hemodynamic parameters with respect to oxidative stress has not been investigated in DMD. Thus, here we aim to utilize DCE-CT to monitor changes in hemodynamic parameters such as blood flow (BF), blood volume (BV), and mean transit time (MTT) which may be affected by nNOS mislocalization. We hypothesize that CT scans will model DMD progression by providing absolute quantification of perfusion. Additionally, we hypothesize that oxidative stress may correlate with DCE-CT perfusion

parameters to replicate the pathologic environment seen in later stages of DMD as mentioned prior.

1.7.2 Study Objectives

1. To compare functional maps of BF, BV, and MTT in the brain, heart, and skeletal muscle between control and DMD group using DCE-CT at two time points, specifically the 4-5 week time point (pre-fibrotic) and 8-10 week time point (fibrotic).
2. To investigate the role of oxidative stress in the heart, brain, and skeletal muscle of murine DMD models at two time points, specifically the 4-5 weeks (pre-fibrotic) and 8-10 weeks (fibrotic) time points, given that oxidative stress is known to cause changes in hemodynamic parameters.

C57bl/10 and *mdx* mice were used for experimental purpose since the intersection of hemodynamic parameters and MPO has not been investigated in DMD. Two time points were selected, the 3-5 week, 8-10 week ones specifically corresponding to the pre-fibrotic and fibrotic conditions respectively.¹⁷ These time points may provide insight into perfusion parameters prior to fatal complications as the disease progresses with respect to oxidative stress. Following DCE-CT imaging, analysis was localized to the brain, heart, and skeletal muscle for region of interests as these are some of the most monitored areas within DMD patients due to their vital functions. To validate DCE-CT findings, histological staining for MPO, Masson's Trichrome, and hematoxylin and eosin (H&E) were performed.

1.8 References

1. Crisafulli, S. *et al.* Global epidemiology of Duchenne muscular dystrophy: An updated systematic review and meta-analysis. *Orphanet J. Rare Dis.* **15**, (2020).
2. Babbs, A. *et al.* From diagnosis to therapy in Duchenne muscular dystrophy. *Biochem. Soc. Trans.* **48**, 813–821 (2020).
3. Lynch, G. S. Proceedings of the Australian Physiological and Pharmacological Society Symposium : ROLE OF CONTRACTION-INDUCED INJURY IN THE MECHANISMS OF MUSCLE DAMAGE IN MUSCULAR DYSTROPHY. *Proc. Aust. Physiol. Pharmacol. Soc.* 537–540 (2010).
4. Chamberlain, J. R. & Chamberlain, J. S. Progress toward Gene Therapy for Duchenne Muscular Dystrophy. *Mol. Ther.* **25**, 1125–1131 (2017).
5. Wells, D. J. Tracking progress: An update on animal models for Duchenne muscular dystrophy. *DMM Dis. Model. Mech.* **11**, 1992–1994 (2018).
6. Mah, J. K. *et al.* A systematic review and meta-analysis on the epidemiology of Duchenne and Becker muscular dystrophy. *Neuromuscul. Disord.* **24**, 482–491 (2014).
7. Grimm, T., Kress, W., Meng, G. & Muller, C. R. Risk assessment and genetic counseling in families with Duchenne muscular dystrophy. *Acta Myol.* **31**, 179–183 (2012).
8. Mollanoori, H., Rahmati, Y., Hassani, B., Havasi Mehr, M. & Teimourian, S. Promising therapeutic approaches using CRISPR/Cas9 genome editing technology in the treatment of Duchenne muscular dystrophy. *Genes Dis.* **8**, 146–156 (2021).
9. Doorenweerd, N. *et al.* Timing and localization of human dystrophin isoform expression provide insights into the cognitive phenotype of Duchenne muscular dystrophy. *Sci. Rep.* **7**, 1–12 (2017).

10. Victor, R. G. *et al.* A phase 3 randomized placebo-controlled trial of tadalafil for Duchenne muscular dystrophy. *Neurology* **89**, 1811–1820 (2017).
11. Adamo, C. M. *et al.* Sildenafil reverses cardiac dysfunction in the mdx mouse model of Duchenne muscular dystrophy. *Proc. Natl. Acad. Sci. U. S. A.* **107**, 19079–19083 (2010).
12. Percival, J. M. *et al.* Sildenafil reduces respiratory muscle weakness and fibrosis in the mdx mouse model of Duchenne muscular dystrophy. *J. Pathol.* **228**, 77–87 (2012).
13. Hoque, R. Sleep-disordered breathing in duchenne muscular dystrophy: An assessment of the literature. *J. Clin. Sleep Med.* **12**, 905–911 (2016).
14. Ciafaloni, E. *et al.* Delayed Diagnosis in Duchenne Muscular Dystrophy: Data from the Muscular Dystrophy Surveillance, Tracking, and Research Network (MD STARnet). *J. Pediatr.* **155**, 380–385 (2009).
15. Birnkrant, D. J. *et al.* Diagnosis and management of Duchenne muscular dystrophy, part 2: respiratory, cardiac, bone health, and orthopaedic management. *Lancet Neurol.* **17**, 347–361 (2018).
16. Nascimento Osorio, A., Medina Cantillo, J., Camacho Salas, A., Madruga Garrido, M. & Vilchez Padilla, J. J. Consensus on the diagnosis, treatment and follow-up of patients with Duchenne muscular dystrophy. *Neurol. (English Ed.)* **34**, 469–481 (2019).
17. Yucel, N., Chang, A. C., Day, J. W., Rosenthal, N. & Blau, H. M. Humanizing the mdx mouse model of DMD: the long and the short of it. *npj Regen. Med.* **3**, (2018).
18. Fischmann, A. & Fischer, D. Neuromuscular imaging in muscular dystrophies and other muscle diseases. *Imaging Med.* **5**, 237–248 (2013).
19. Hathout, Y. *et al.* Clinical utility of serum biomarkers in Duchenne muscular

- dystrophy. *Clin. Proteomics* **13**, 1–9 (2016).
20. Cacchiarelli, D. *et al.* miRNAs as serum biomarkers for Duchenne muscular dystrophy. *EMBO Mol. Med.* **3**, 258–265 (2011).
 21. Nilipour, Y. The art of muscle biopsy in the new genetic era: A narrative review. *Iran. J. Child Neurol.* **13**, 7–17 (2019).
 22. Shi, X. & Garry, D. J. Muscle stem cells in development, regeneration, and disease. *Genes Dev.* **20**, 1692–1708 (2006).
 23. Mavrogeni, S. I., Markousis-mavrogenis, G., Papavasiliou, A., Papadopoulos, G. & Kolovou, G. Chapter 3. **1687**, (2018).
 24. Doorenweerd, N. *et al.* Decreased cerebral perfusion in Duchenne muscular dystrophy patients. *Neuromuscul. Disord.* **27**, 29–37 (2017).
 25. Hawkins, B. T. & Davis, T. P. The blood-brain barrier/neurovascular unit in health and disease. *Pharmacol. Rev.* **57**, 173–185 (2005).
 26. Bushby, K. M. D. *et al.* Deletion Status and Intellectual Impairment in Duchenne Muscular Dystrophy. *Dev. Med. Child Neurol.* **37**, 260–269 (1995).
 27. Angelini, C. & Pinzan, E. Advances in imaging of brain abnormalities in neuromuscular disease. *Ther. Adv. Neurol. Disord.* **12**, 1–24 (2019).
 28. Anderson, J. L., Head, S. I., Rae, C. & Morley, J. W. Brain function in Duchenne muscular dystrophy. *Brain* **125**, 4–13 (2002).
 29. Meyers, T. A. & Townsend, D. W. Cardiac pathophysiology and the future of cardiac therapies in duchenne muscular dystrophy. *Int. J. Mol. Sci.* **20**, (2019).
 30. Hamer, P. W., McGeachie, J. M., Davies, M. J. & Grounds, M. D. Evans Blue Dye as an in vivo marker of myofibre damage: Optimising parameters for detecting initial myofibre membrane permeability. *J. Anat.* **200**, 69–79 (2002).

31. Johnstone, V. P. A., Viola, H. M. & Hool, L. C. Dystrophic cardiomyopathy—potential role of calcium in pathogenesis, treatment and novel therapies. *Genes (Basel)*. **8**, (2017).
32. Law, M. L., Cohen, H., Martin, A. A., Angulski, A. B. B. & Metzger, J. M. Dysregulation of Calcium Handling in Duchenne Muscular Dystrophy-Associated Dilated Cardiomyopathy: Mechanisms and Experimental Therapeutic Strategies. *J. Clin. Med.* **9**, 520 (2020).
33. Jouvion, G. The Female mdx Mouse: An Unexpected Vascular Story. *J. Neurol. Neuromedicine* **1**, 41–53 (2016).
34. Mak, I. T. *et al.* Deficiency in gp91Phox (NOX2) Protects against Oxidative Stress and Cardiac Dysfunction in Iron Overloaded Mice. *Hearts* **1**, 117–125 (2020).
35. Pal, R. *et al.* Src-dependent impairment of autophagy by oxidative stress in a mouse model of Duchenne muscular dystrophy. *Nat. Commun.* **5**, 1–10 (2014).
36. Smith, L. R., Hammers, D. W., Sweeney, H. L. & Barton, E. R. Increased collagen cross-linking is a signature of dystrophin-deficient muscle. *Muscle and Nerve* **54**, 71–78 (2016).
37. Nitahara-Kasahara, Y., Takeda, S. & Okada, T. Inflammatory predisposition predicts disease phenotypes in muscular dystrophy. *Inflamm. Regen.* **36**, 3–7 (2016).
38. Farini, A. *et al.* Fibrosis Rescue Improves Cardiac Function in Dystrophin-Deficient Mice and Duchenne Patient–Specific Cardiomyocytes by Immunoproteasome Modulation. *Am. J. Pathol.* **189**, 339–353 (2019).
39. Naidoo, M. & Anthony, K. Dystrophin Dp71 and the Neuropathophysiology of Duchenne Muscular Dystrophy. *Mol. Neurobiol.* **57**, 1748–1767 (2020).
40. Goodnough, C. L. *et al.* Lack of dystrophin results in abnormal cerebral diffusion and perfusion in vivo. *Neuroimage* **102**, 809–816 (2014).

41. Bowler, J. V. Vascular cognitive impairment. *Neurol. Pract.* **76**, (2005).
42. Uchino, M. *et al.* Localisation and characterisation of dystrophin in the central nervous system of controls and patients with Duchenne muscular dystrophy. *J. Neurol. Neurosurg. Psychiatry* **57**, 426–429 (1994).
43. Anand, K. & Dhikav, V. Hippocampus in health and disease: An overview. *Ann. Indian Acad. Neurol.* **15**, 239–246 (2012).
44. Cyrulnik, S. E. & Hinton, V. J. Duchenne muscular dystrophy: A cerebellar disorder? *Neurosci. Biobehav. Rev.* **32**, 486–496 (2008).
45. Rae, M. G. & O'Malley, D. Cognitive dysfunction in Duchenne muscular dystrophy: A possible role for neuromodulatory immune molecules. *J. Neurophysiol.* **116**, 1304–1315 (2016).
46. Kato, T. *et al.* Increased cerebral choline-compounds in Duchenne muscular dystrophy. *Neuroreport* **8**, 1435–1437 (1997).
47. Xu, S. *et al.* Abnormalities in brain structure and biochemistry associated with mdx mice measured by in vivo MRI and high resolution localized 1H MRS. *Neuromuscul. Disord.* **25**, 764–772 (2015).
48. Forcina, L., Pelosi, L., Miano, C. & Musarò, A. Insights into the pathogenic secondary symptoms caused by the primary loss of dystrophin. *J. Funct. Morphol. Kinesiol.* **2**, (2017).
49. Klingler, W., Jurkat-Rott, K., Lehmann-Horn, F. & Schleip, R. The role of fibrosis in Duchenne muscular dystrophy. *Acta Myol.* **31**, 184–195 (2012).
50. Gimbel, M. L., Hunt, T. K. & Hussain, M. Z. Lactate controls collagen gene promoter activity through pADPR. *J. Am. Coll. Surg.* **191**, S79 (2000).
51. Emery, A. E. H. Muscle lactate dehydrogenase isoenzymes in hereditary myopathies. *J. Neurol. Sci.* **7**, 137–148 (1968).

52. Terrill, J. R. *et al.* Oxidative stress and pathology in muscular dystrophies: Focus on protein thiol oxidation and dysferlinopathies. *FEBS J.* **280**, 4149–4164 (2013).
53. Lindsay, A., McCourt, P. M., Karachunski, P., Lowe, D. A. & Ervasti, J. M. Xanthine oxidase is hyper-active in Duchenne muscular dystrophy. *Free Radic. Biol. Med.* **129**, 364–371 (2018).
54. Boittin, F. X., Shapovalov, G., Hirn, C. & Ruegg, U. T. Phospholipase A2-derived lysophosphatidylcholine triggers Ca²⁺ entry in dystrophic skeletal muscle fibers. *Biochem. Biophys. Res. Commun.* **391**, 401–406 (2010).
55. Choi, M. H., Ow, J. R., Yang, N. Di & Taneja, R. Oxidative Stress-Mediated Skeletal Muscle Degeneration: Molecules, Mechanisms, and Therapies. *Oxid. Med. Cell. Longev.* **2016**, (2016).
56. Strzepa, A., Pritchard, K. A. & Dittel, B. N. Myeloperoxidase: A new player in autoimmunity. *Cell. Immunol.* **317**, 1–8 (2017).
57. Block, M. S. & Rowan, B. G. Hypochlorous Acid: A Review. *J. Oral Maxillofac. Surg.* **78**, 1461–1466 (2020).
58. Cai, H., Chuang, C. Y., Hawkins, C. L. & Davies, M. J. Binding of myeloperoxidase to the extracellular matrix of smooth muscle cells and subsequent matrix modification. *Sci. Rep.* **10**, 1–13 (2020).
59. Dombernowsky, N. W., Ölmestig, J. N. E., Witting, N. & Kruuse, C. Role of neuronal nitric oxide synthase (nNOS) in Duchenne and Becker muscular dystrophies – Still a possible treatment modality? *Neuromuscul. Disord.* **28**, 914–926 (2018).
60. Eiserich, J. P. *et al.* Myeloperoxidase, a leukocyte-derived vascular NO oxidase. *Science (80-.).* **296**, 2391–2394 (2002).
61. Baldus, S. *et al.* Myeloperoxidase enhances nitric oxide catabolism during myocardial ischemia and reperfusion. *Free Radic. Biol. Med.* **37**, 902–911 (2004).

62. Gouloupoulou, S. Calpain A Novel Mediator of MPO (Myeloperoxidase)-Induced Endothelial Dysfunction. *Contemp. Hypn.* **19**, 147 (2002).
63. Sander, M. *et al.* Functional muscle ischemia in neuronal nitric oxide synthase-deficient skeletal muscle of children with Duchenne muscular dystrophy. *Proc. Natl. Acad. Sci. U. S. A.* **97**, 13818–13823 (2000).
64. Narayanan, I., Das, S., Vaishnava, S. & Sriramachari. Duchenne muscular dystrophy. *Indian Pediatr.* **7**, 429–441 (1970).
65. Blottner, D. & Lück, G. Nitric oxide synthase (NOS) in mouse skeletal muscle development and differentiated myoblasts. *Cell Tissue Res.* **292**, 293–302 (1998).
66. Rando, T. A. Role of nitric oxide in the pathogenesis of muscular dystrophies: A ‘two hit’ hypothesis of the cause of muscle necrosis. *Microsc. Res. Tech.* **55**, 223–235 (2001).
67. Timpani, C. A., Hayes, A. & Rybalka, E. Therapeutic strategies to address neuronal nitric oxide synthase deficiency and the loss of nitric oxide bioavailability in Duchenne Muscular Dystrophy. *Orphanet J. Rare Dis.* **12**, 1–11 (2017).
68. Ito, K. *et al.* Smooth muscle-specific dystrophin expression improves aberrant vasoregulation in mdx mice. *Hum. Mol. Genet.* **15**, 2266–2275 (2006).
69. Crosbie, R. H., Barresi, R. & Campbell, K. P. Loss of sarcolemma nNOS in sarcoglycan-deficient muscle. *FASEB J.* **16**, 1786–1791 (2002).
70. Chen, Y. W. *et al.* Early onset of inflammation and later involvement of TGF β in Duchenne muscular dystrophy. *Neurology* **65**, 826–834 (2005).
71. Scaffidi, P., Misteli, T. & Bianchi, M. E. Erratum: Release of chromatin protein HMGB1 by necrotic cells triggers inflammation (Nature (2002) 418 (191-195)). *Nature* **467**, 622 (2010).

72. Rudolph, T. K. *et al.* Myeloperoxidase deficiency preserves vasomotor function in humans. *Eur. Heart J.* **33**, 1625–1634 (2012).
73. Pool, J. L. Magnetic resonance imaging. *Biomed. Instrum. Technol.* **36**, 341–346 (2002).
74. Jahng, G. H., Li, K. L., Ostergaard, L. & Calamante, F. Perfusion magnetic resonance imaging: A comprehensive update on principles and techniques. *Korean J. Radiol.* **15**, 554–577 (2014).
75. Adam, A. & Ahmed, A. MRI LIMITATIONS : THE MAIN ASPECTS AND RESOLVING TECHNIQUES MRI LIMITATIONS : THE MAIN ASPECTS AND RESOLVING TECHNIQUES Rahma Abdalla. 1–4 (2020).
76. Karim, H., Schmidt, B., Dart, D., Beluk, N. & Huppert, T. Functional near-infrared spectroscopy (fNIRS) of brain function during active balancing using a video game system. *Gait Posture* **35**, 367–372 (2012).
77. Rupawala, M., Dehghani, H., Lucas, S. J. E., Tino, P. & Cruse, D. Shining a light on awareness: A review of functional near-infrared spectroscopy for prolonged disorders of consciousness. *Front. Neurol.* **9**, 1–17 (2018).
78. Brandão, P. *et al.* A review of Medical Doppler US. *J. Med. Ultrasound* 115–117 (2018) doi:10.4103/JMU.JMU.
79. Maddahi, J. & Packard, R. R. S. Cardiac PET perfusion tracers: Current status and future directions. *Semin. Nucl. Med.* **44**, 333–343 (2014).
80. Manabe, O., Naya, M., Aikawa, T. & Yoshinaga, K. ¹⁵O-labeled Water is the Best Myocardial Blood Flow Tracer for Precise MBF Quantification. *Ann. Nucl. Cardiol.* **5**, 69–72 (2019).
81. O'Connor, J. P. B. *et al.* Dynamic contrast-enhanced imaging techniques: CT and MRI. *Br. J. Radiol.* **84**, (2011).

82. McGreevy, J. W., Hakim, C. H., McIntosh, M. A. & Duan, D. Animal models of Duchenne muscular dystrophy: From basic mechanisms to gene therapy. *DMM Dis. Model. Mech.* **8**, 195–213 (2015).
83. Li, D. *et al.* Sarcolemmal nNOS anchoring reveals a qualitative difference between dystrophin and utrophin. *J. Cell Sci.* **123**, 2008–2013 (2010).
84. Kleopa, K. A., Drousiotou, A., Mavrikiou, E., Ormiston, A. & Kyriakides, T. Naturally occurring utrophin correlates with disease severity in Duchenne muscular dystrophy. *Hum. Mol. Genet.* **15**, 1623–1628 (2006).
85. Kennedy, T. L. *et al.* Utrophin influences mitochondrial pathology and oxidative stress in dystrophic muscle. *Skelet. Muscle* **7**, 22 (2017).
86. Tan, N. & Lansman, J. B. Utrophin regulates modal gating of mechanosensitive ion channels in dystrophic skeletal muscle. *J. Physiol.* **592**, 3303–3323 (2014).
87. Collins, C. A. & Morgan, J. E. Duchenne’s muscular dystrophy: Animal models used to investigate pathogenesis and develop therapeutic strategies. *Int. J. Exp. Pathol.* **84**, 165–172 (2003).
88. Khouzami, L. *et al.* Delayed cardiomyopathy in dystrophin deficient mdx mice relies on intrinsic glutathione resource. *Am. J. Pathol.* **177**, 1356–1364 (2010).
89. Frinchi, M., Morici, G., Mudó, G., Bonsignore, M. R. & Di Liberto, V. Beneficial role of exercise in the modulation of mdx muscle plastic remodeling and oxidative stress. *Antioxidants* **10**, 1–55 (2021).
90. van Putten, M. *et al.* Natural disease history of the D2-mdx mouse model for Duchenne muscular dystrophy. *FASEB J.* **33**, 8110–8124 (2019).

Chapter 2

2 In-vivo whole-body CT perfusion imaging

2.1 Introduction

Medical imaging is the process of creating visual representations of the body, including organs and tissues, to facilitate analysis in clinic to diagnose or offer medical intervention. Neuromuscular disorders, such as DMD, depend on the accuracy and precision of diagnostic measures. Often diagnosis is challenging because of patient variability and poor specificity of validation techniques. Currently, there is an increasing need to implement non-invasive imaging modalities in routine care to assess DMD disease diagnosis and progression. In clinic, health care professionals may use ultrasound, echocardiography, PET, fNIRS, MRI, or even DCE-CT as an imaging modality of choice to view and characterize disease progression in patients.

Ultrasound is often used when imaging neuromuscular disorders in children due to the absence of ionizing radiation, availability, and low cost. It can quickly identify fatty degeneration, atrophic changes, and muscle thickness. However, ultrasound is limited to the observation of superficial muscle groups. Furthermore, there is low intra-observer, and inter-observer agreement since the diagnosis and prognosis when observing the echogenicity and muscle morphology are highly dependent on the manual dexterity of the operator.¹ One study tested quantitative backscatter analysis (QBA) and grayscale levels (GSL) values from a group of 6 muscles in boys aged 2 to 14 years (n=25). Results indicated that although QBA and GSL have similar results with respect to age and function analysis, they were unable to image the quadriceps and medial gastrocnemius muscle appropriately due to plateauing of echo intensity. Some possible explanations as to why this occurred focused on the pathology of the disease, specifically the fact that hypertrophy and pseudohypertrophy can alter echo intensity which can make it hard to discern whether echo intensity or age is contributing to the disease state.² Similarly, echocardiography has been previously used to study cardiac function in patients, to detect the presence of DCM and sinus tachycardia. While this method has made advances in characterizing fibrosis, necrosis, and hypertrophy within certain tissues and organs, it

possesses some limitations.³ In an investigation pertaining to serial images taken from left ventricular segments, in patients aged 3.6 to 19.9 years of age, over half of echocardiograms were deemed suboptimal at the 13-year time point with more than 30% of segments inadequately captured. Further, by 15 years of age, around 78% of images were suboptimal⁴. As such, echocardiographs are limited in image quality with increasing age in DMD patients.

Positron emission tomography (PET) has been used to study wall motion, cardiac metabolism, and function in DMD patients. Further, PET has been used to demonstrate that there's increased glucose uptake in the left ventricle of patients, this is supported by findings which report the presence of DCM.⁵ Limitations of PET imaging include the fact that it is dependent on blood flow for accurate radiotracer uptake in tissues and uptake of radiotracer depends on the cells' metabolic demands. Radiation encountered per PET scan usually contains higher amounts when compared to DCE-CT.⁶ In addition, the inflammation of tissue can limit tracer uptake thus hindering results of studies⁵.

Functional near-infrared spectroscopy (fNIRS) may be used to evaluate hemodynamic responses in patients. It works by calculating physiologic parameters non-invasively based on the absorption spectrum of deoxy and oxy hemoglobin.⁷ fNIRS has been shown to be cost effective, and useful for acute and longitudinal studies. One paper revealed that muscle oxygenation was impaired in DMD patients after undergoing a routine six-minute walk test⁸. Despite its usefulness in classifying oxygenation within various tissue fNIRS suffers from lower spatial resolution and limited depth of recording⁹.

Magnetic Resonance is able to view soft tissue well and can evaluate various features of skeletal muscle. This modality can determine fatty degeneration using T1-weighted images and recognize large decreases in overall muscle volume. T2-weighted images are beneficial when muscle edema is present. T1-weighted images primarily focus on rendering images of adipose tissue by targeting proton energy within fatty tissue. In contrast, T2-weighted images can render images pertaining to tissues containing both fat and water based on proton energy emitted.¹⁰ In recent years MRI, more specifically cardiac magnetic resonance, has served to detect cardiac dysfunction in DMD patients.

Cardiac magnetic resonance allows for three-dimensional volumetric measurement analysis, to detect overall heart function and strain.¹¹

Lastly, Computer Tomography (CT) has been used to monitor changes in skeletal muscle and organs in a wide array of disorders. Past literature has shown that adipose deposition in replacement of skeletal muscle is less identifiable on CT perfusion scans due to a loss of contrast within the tissue. Poor contrast in soft tissue can lead to challenges for identifying muscle degeneration.¹² However, recent work has cited the presence of muscle edema prior to damage, which is where the use and role of DCE-CT in clinic is important for DMD assessment.¹³ The primary advantage of DCE-CT is the linear relationship between contrast agent concentration and X-ray attenuation.¹⁴ In addition, DCE-CT is relatively cheap, widely available, and has high spatial resolution. These high resolution images have been shown to have greater reproducibility than PET or MRI. One limitation for DCE-CT includes the use of ionizing radiation approximately 1-2 mSv/scan, however many physicians agree that the risk of adverse effects of radiation are minimal compared to the benefits in terms of disease monitoring and diagnosis.¹⁴ Parents and younger patients are more compliant with this modality as exams require little scan time and have a low cost burden. More recently, family members and healthcare providers have looked towards using DCE-CT long-term to monitor disease progression, and accurate diagnosis in other conditions such as renal cancer; however there haven't been many studies conducted pertaining to DMD. Thus, here we aim to study whole-body DCE-CT imaging and compare results with findings of oxidative stress.

2.2 Materials and Methods

All studies and experiments were completed at Lawson Health Research Institute at St. Joseph's Health Care in London, Ontario. Animal use protocol, AUP 2018-140, was approved by the Animal Use Subcommittee at Western University and complied with the Canadian Council on Animal Care (CCAC) guidelines (Appendix A).

2.2.1 Study Population

Wild-type (*C57bl/10*) were purchased from Charles River and Jackson Laboratories (JAX) (Bar Harbor, ME) as they are the appropriate background control to the *mdx*

mouse model, whereas *mdx*, also known as, *mdx/utrn*^{+/+} mice were bred in house using breeding pairs of *C57bl/10* and *mdx/utrn*^{+/-} obtained from JAX. Housing conditions for the colonies were controlled (19-23 °C, 12-hour light/dark cycles), mice were allowed food and water *ad libitum*. All mice used were bred using an in-house protocol (AUP2017-038) in accordance with CCAC guidelines and were genotyped by the Hoffman lab. Two populations were studied where *in-vivo* imaging (n=3-5 mice/time point/genotype) and *ex-vivo* histology cohorts (n=3 mice/time point/genotype), which will be referred to as the DCE-CT and immunohistochemistry (IHC) cohort, respectively.

2.2.2 DCE- CT Imaging Protocol and Analysis Overview

Mice of mixed sex were DCE-CT scanned acutely at 3-5 weeks, and 8-10 weeks, these points correspond to the pre-fibrotic and fibrotic time points respectively. Prior to DCE-CT imaging mice were weighed and given a 3-4% oxygen-balanced isoflurane mixture delivered at a rate of 1L/min and inhaled via nose cone to induce anesthesia. Following induction, mice were maintained with a 1.5-2.5% oxygen-balanced isoflurane mixture delivered at a flow rate of 1L/min. Following anatomical axial scans, each mouse received weight dependent dose between 140 – 200 µL of Conray 43 contrast agent (diluted 1:2 with sterile saline) at an injection rate of 0.25 ml/min using an infusion pump (New Era Pump Systems Inc) via tail vein catheter for 10 minutes.³² CT perfusion software (CTP_W15) was used to quantify blood flow (BF), blood volume (BV) and mean transit time (MTT) using a Johnson-Wilson-Lee deconvolution algorithm to generate the functional maps.³⁴ Regions of interest (ROIs) were drawn around the entire cross-sectional slice of the hind limb, entire width of the brain, and focused on the lateral area of myocardium tissue. Care was taken to exclude artifacts such as bone fragments. Data analysis of results was conducted using a blinded model where age, sex, and genotype were unknown.

2.2.3 Histology

2.2.3.1 Tissue Preparation

In addition to the DCE-CT cohort, mice within the IHC cohort were sacrificed using cervical dislocation following CO₂ gas euthanasia to supplement data. Tissues were cut in

the same orientation and fixed in 10% formalin for 24-48 hrs. Tissues were later paraffin embedded and processed at the Molecular Pathology facility (Robarts Research Institute, London, ON) and cut into sections 10 μm thick.

2.2.3.2 Immunohistochemistry Protocol

The following was adapted and modified from Abcam's fluorescent staining protocol. Tissue sections were deparaffinized and rehydrated using a series of xylene and ethanol washes prior to heat-mediated antigen retrieval in citrate buffer for 1 hr. Slides were cooled to room temperature, Background Sniper was applied for 8 minutes to reduce nonspecific background staining. Tissue sections were then incubated overnight 4°C with either primary anti-MPO (1:200, Abcam), or no antibody. All antibodies were diluted using 1% bovine serum albumin (BSA) in phosphate buffer saline (PBS). Following washing with 4 x PBS, Alexafluor 594 Goat-anti rabbit IgG (1:500) secondary antibody was incubated for 2 h at room temperature and used to visualize the primary antibody. Following, copper sulfate pentahydrate, $\text{Cu}_2\text{SO}_4 \cdot 5\text{H}_2\text{O}$, was applied for 10 minutes to block/prevent red blood cell autofluorescence. 0.1% Sudan Black B was applied for 2-3 minutes to dampen autofluorescence due to fat cells. ProLong Gold anti-fade with 4',6-diamidino-2-phenylindole (DAPI) (Life Technologies) was added prior to coverslips to visualize nuclei on slides. Masson's trichrome and H&E staining (completed by Molecular Pathology Lab at Robarts Research Institute, London, ON) was used to visualize for pathological features and was performed solely for qualitative analysis.

2.2.3.3 Microscopy and Image Analysis

Images were acquired using an epifluorescence microscope (Nikon Eclipse Ts2R) using NIS Elements Microscope Image Software for MPO results. Images were taken at 60x magnification for each tissue section (n=3 images/tissue section). Quantitative assessment of MPO signal in both wild-type and *mdx* mice were performed using optimized parameters during thresholding in ImageJ (LOCI, Wisconsin, USA). Masson's trichrome and H&E staining was captured using a Zeiss Axioskop 50 Microscope at 20x magnification and analyzed using Eclipse Image Software.

2.2.4 Statistical Analysis

Microsoft Excel Version 16.5 (Redmond, Washington, United States) was used to perform statistical analysis. Results are displayed as mean \pm standard deviation (SD). Welch's two-tailed t-tests were used to create comparisons between groups. For hemodynamic parameters and histology data a P-value of less than 0.1 was considered significant considering that hemodynamic parameters could be upregulated or downregulated. Figure legends include replicate numbers.

2.3 Results

For this study, mice of mixed sex were used for CT scans and histologic analysis. A total of 15 mice were used. For the 3-5 week *mdx* group 4 females and one male mouse was used. For the 3-5 week *C57bl/10* group 2 females, and 2 males mice were used, For the 8-10 week *mdx* group 2 females and 1 male mouse was used. For the 8-10 week *C57bl/10* group 1 female, and 2 male mice were used. Prior to CT scans mice were weighed and all vital signs were meticulously monitored. At 4-5 weeks *C57bl/10* mice had an average weight of 18.5 ± 1.7 g, and *mdx* mice had an average weight of 17.8 ± 2.4 g. At 8-10 weeks of age weeks *C57bl/10* mice had an average weight of 23 ± 4.3 g and *mdx* mice had an average weight of 25 ± 1.0 g.

2.3.1 Arterial Enhancement Curves display notable differences between the 4-5 week pre-fibrotic time point and 8-10 week fibrotic time point in DMD

CTP_W15 software was used to generate arterial enhancement curves measured in Hounsfield units (HU). Arterial enhancement curves were defined by placing a ROI in the left ventricle of the heart. Data from these curves were used to generate hemodynamic maps and calculate tissue perfusion defined by ROIs. Interestingly, the time to peak (TTP) at the 4-5 week time point occurs much later, with a delay of approximately 16 seconds (s), in *mdx* mice than control group *C57bl/10*. Furthermore, a 14.00% difference in TTP at the 4-5 week time point was observed; values were quantified as $376.45 \pm$

87.76 (HU) and 330.13 ± 40.65 (HU) for *mdx* and *C57bl/10* groups respectively (Figure 2.1). In contrast, TTP for the arterial enhancement curve at the 8-10 week time point occurs at relatively the same time point, approximately 50 s, and yields relatively similar results, 238.13 ± 29.27 (HU) for the *mdx* group and 250.28 ± 50.26 for the *C57bl/10* group (Figure 2.2).

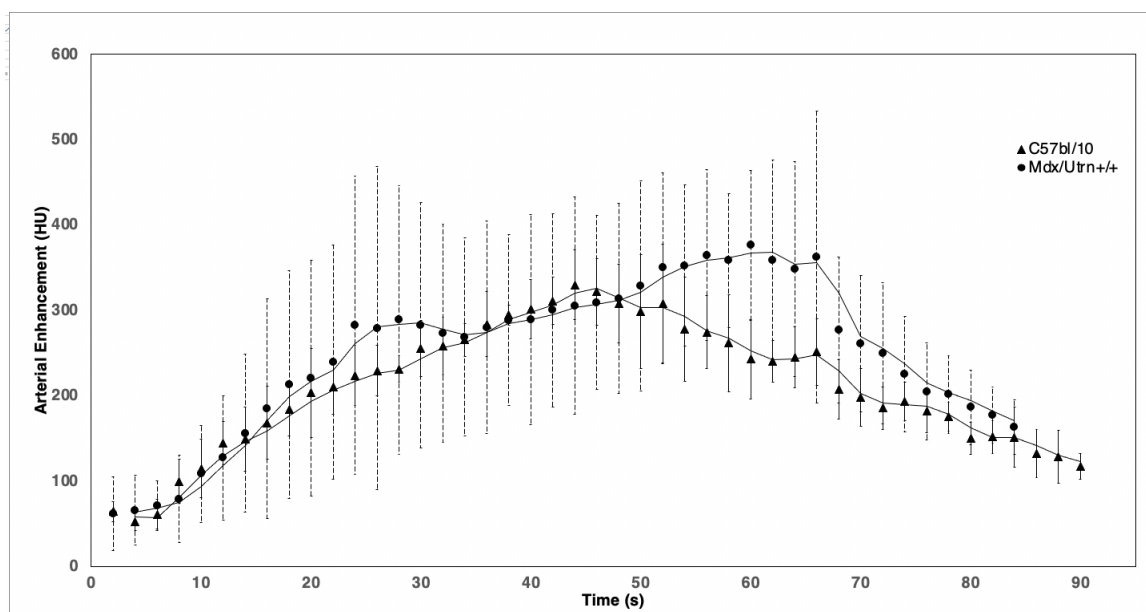


Figure 2.1 Average arterial enhancement curve of *C57bl/10* mice (n=4) compared to *mdx* mice (n=5) at the 4-to-5-week time point

DCE-CT arterial enhancement curves were generated using CTP_W15 software by placing ROI in left ventricle of heart. Arterial Enhancement values (HU) \pm SD were obtained every 2 seconds during an overall period of approximately 90 seconds.

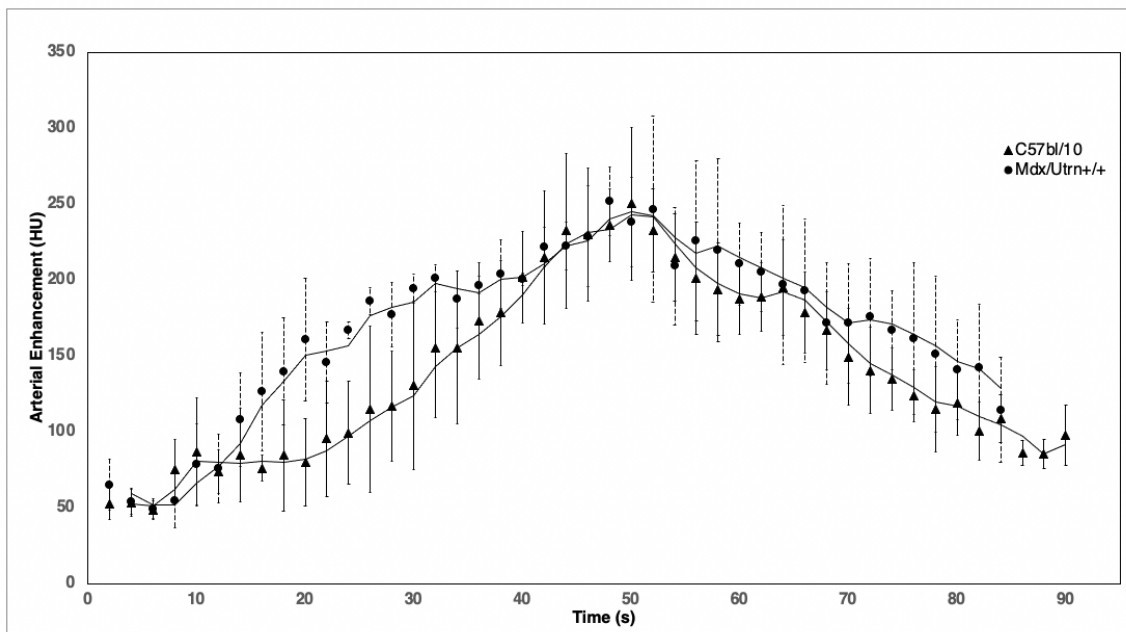


Figure 2.2 Average arterial enhancement curve of *C57bl/10* mice (n=3) compared to *mdx* mice (n=3) at the 8-to-10-week time point

DCE-CT arterial enhancement curves were generated using CTP_W15 software by placing ROI in left ventricle of heart. Arterial Enhancement values (HU) \pm SD were obtained every 2 seconds during an overall period of approximately 90 seconds.

2.3.2 Increases in blood flow and blood volume deemed not significant in DMD brain tissue at 4-5 weeks of age

Mdx mice qualitatively depict higher BV (ml/100g) and BF (ml/min/100g) within brain regions when compared to *C57bl/10* mice at the 4-5 week time point, also herein referred to as the pre-fibrotic time point and early time point (Figure 2.3). Whereas *mdx* mice qualitatively depict similar BV and BF within brain regions at the 8-10 week time point when compared to *C57bl/10* mice; despite relatively longer MTT in certain *mdx* brain regions (Figure 2.4). Blood volume and blood flow measurements were taken with units of ml/100 g, and ml/min/100g of tissue respectively.

Upon ROI perfusion calculation, BV and BF were noted to both increase by 17.00%, and 16.10%, respectively when compared between *mdx* and *C57bl/10* groups at 4-5 weeks. When analyzed further, did not meet significance for BF ($p=0.14$) and BV ($p=0.13$).

Interestingly, MTT despite not reaching significance was noted to decrease between *mdx* and *C57bl/10* groups by 7.90% ($p=0.34$) (Figures 2.9, 2.11, and 2.13).

In contrast, at the 8-10 week time point, herein also noted as the late time point, BF, BV, and MTT did not reach significance. However, notable trends were observed. At this later time point, BF, BV, and MTT were found to decrease by 11.10% ($p=0.68$), 29.29% ($p=0.45$), 55.90% ($p=0.24$) respectively when comparing *mdx* mice to the *C57bl/10* group (Figures 2.10, 2.12, and 2.14).

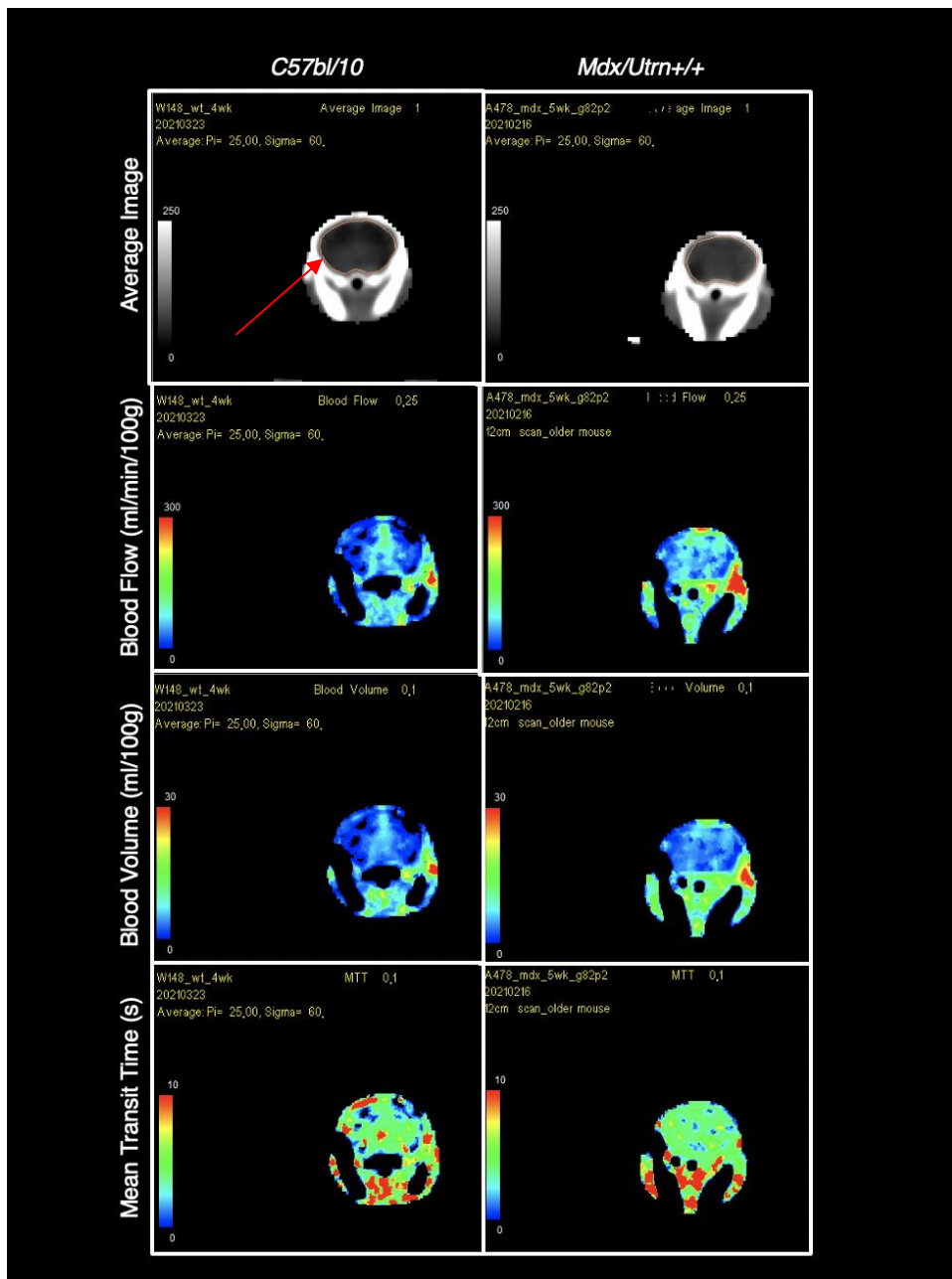


Figure 2.3 Comparison between *C57bl/10* and *mdx* brain regions with respect to blood flow (ml/min/100g), blood volume (ml/100g), and mean transit time (s) at the 4-5 week time point (n=1 biological and n=1 technical replicate per genotype group). *Mdx* qualitatively depict higher blood volume (ml/100g), and blood flow (ml/min/100g) within brain regions when compared to *C57bl/10* mice. Mean transit time (s) is visually observed to decrease. Following DCE-CT protocol, maps were generated using a Johnson-Wilson-Lee deconvolution model (n=4-5 mice/genotype). Red arrow points to ROI drawn in orange placed around the widest section of the brain captured and

encompassed both grey and white matter. Care was taken to exclude sections of bone fragment. *Mdx/Utrn*^{+/+} = *Mdx*, and *C57bl/10*=wild-type mice

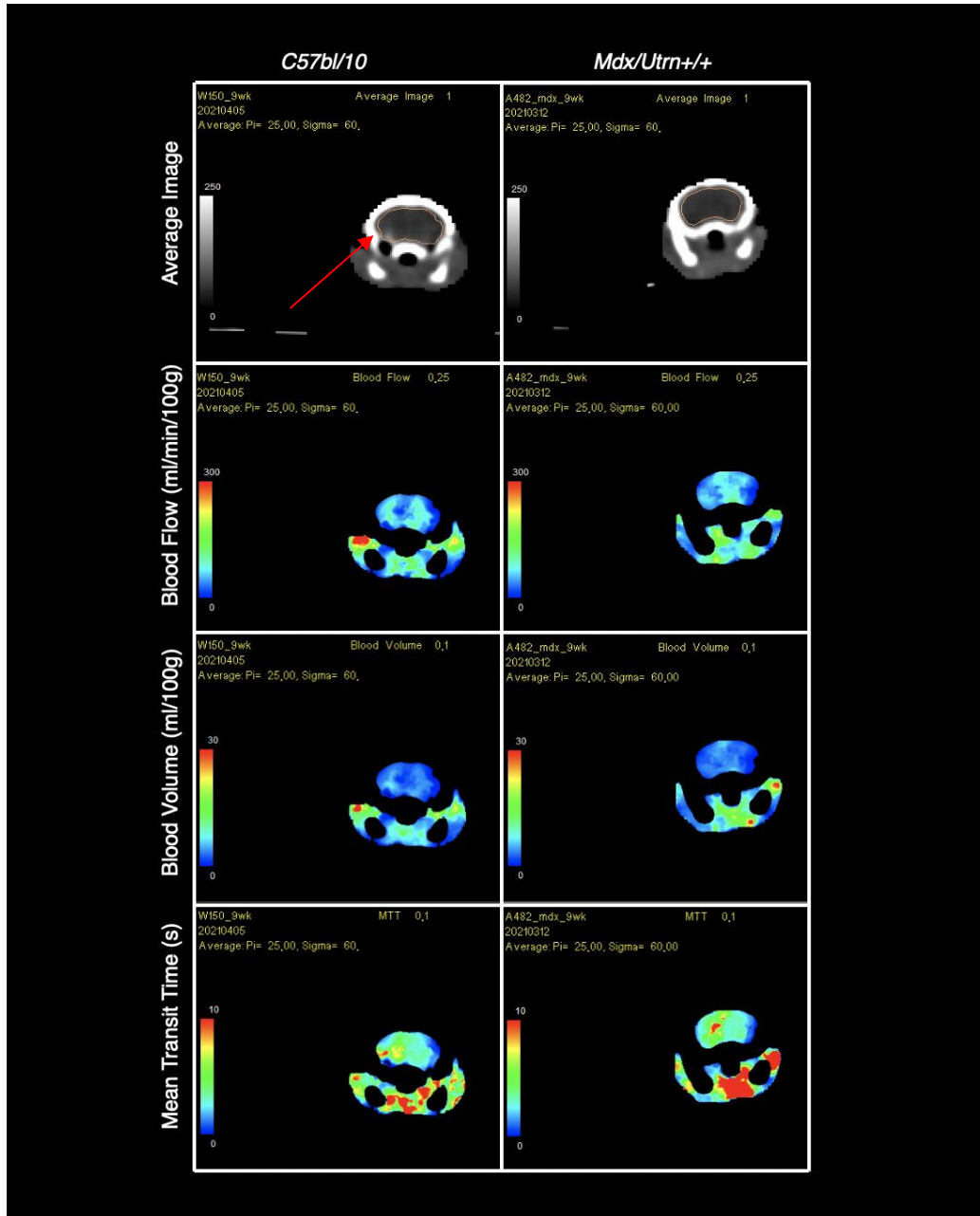


Figure 2.4 Comparison between *C57bl/10* and *mdx* brain regions with respect to blood flow (ml/min/100g), blood volume (ml/100g), and mean transit time (s) at the

8-10 week time point (n=1 biological and n=1 technical replicate per genotype group).

Mdx qualitatively depict decreases in blood volume (ml/100g), and blood flow (ml/min/100g) within brain regions when compared to *C57bl/10* mice. Mean transit time (s) is visually observed to increase. Following DCE-CT protocol, maps were generated using a Johnson-Wilson-Lee deconvolution model (n=3 mice/genotype). Red arrow points to ROI drawn in orange placed around the widest section of the brain captured and encompassed both grey and white matter. Care was taken to exclude sections of bone fragment. *Mdx/Utrn*^{+/+} = *Mdx*, and *C57bl/10*=wild-type mice

2.3.3 Changes in hemodynamic parameters within the myocardium are deemed not statistically significant at the 4-5 week and 8-10 week time points in DMD

Mdx mice qualitatively depict higher blood volume, and blood flow within cardiac regions when compared to *C57bl/10* mice at the 4-5 week time point (Figure 2.5). In contrast, *mdx* mice qualitatively depict lower blood volume, and blood flow within regions of the heart when compared to *C57bl/10* mice at the 8-10 week time point. (Figure 2.6)

Upon ROI perfusion calculation, BV and BF were noted to both increase by 9.47%, and 8.76%, respectively when compared between *mdx* and *C57bl/10* groups at 4-5 weeks. When analyzed further, data did not meet significance for both BF (p=0.29) and BV (p=0.22). In addition, MTT was noted to decrease between *mdx* and *C57bl/10* groups by 2.59% (p=0.78) (Figures 2.9, 2.11, and 2.13).

Similar to the prior time point, at 8-10 weeks, BF, BV, and MTT failed to reach significance. However, a difference in trends was observed. At this time point while BF was noted to increase by 10.03% (p=0.49), both BV and MTT were found to decrease. Specifically, BV decreased by 20.31% (p=0.32), and MTT by 16.67% (p=0.32) between groups (Figures 2.10, 2.12, and 2.14).

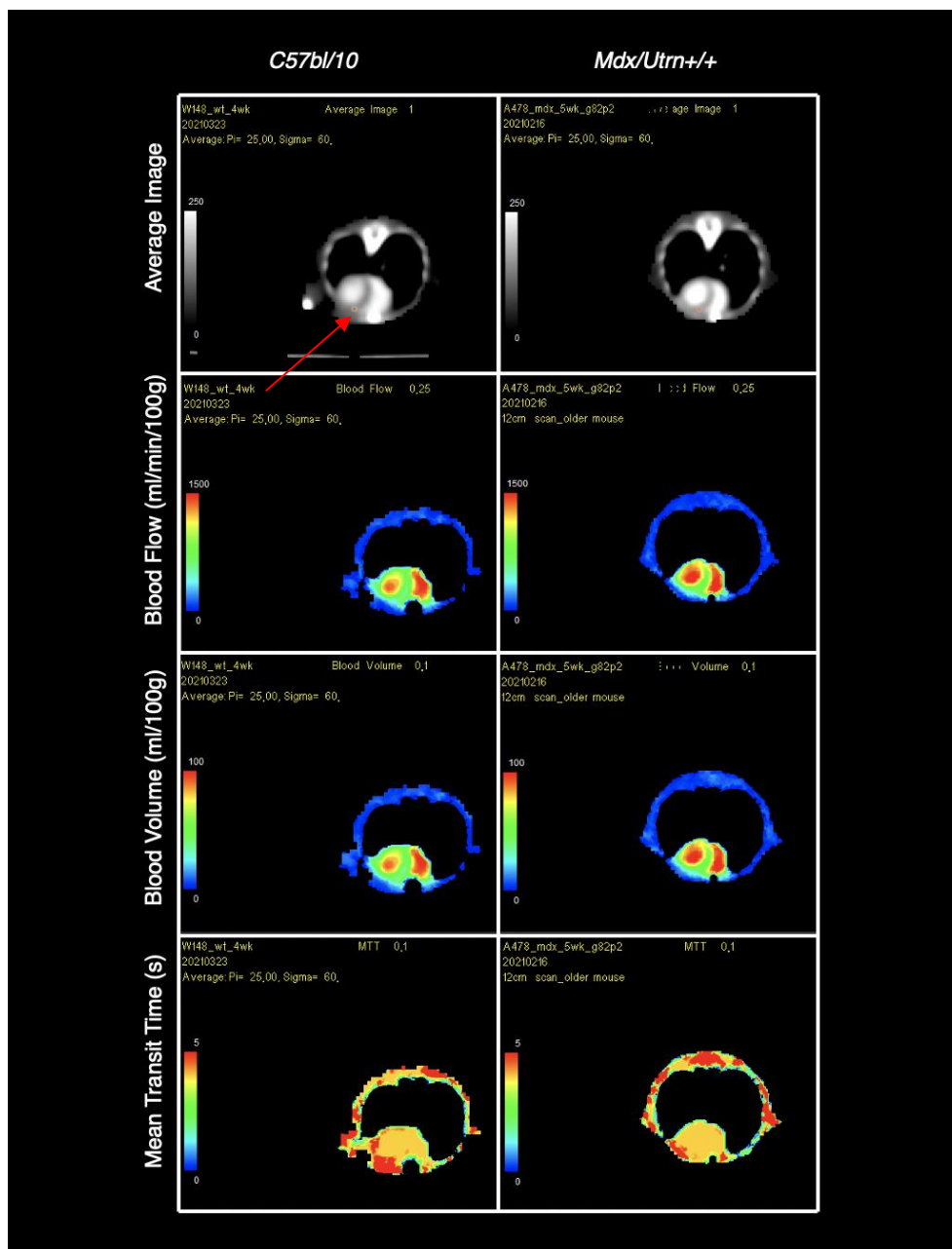


Figure 2.5 Comparison between *C57bl/10* and *mdx* myocardium regions with respect to blood flow (ml/min/100g), blood volume (ml/100g), and mean transit time (s) at the 4-5 week time point (n=1 biological and n=1 technical replicate per genotype group).

Mdx qualitatively depicts increases in blood volume (ml/100g), and blood flow (ml/min/100g) within regions of the heart when compared to *C57bl/10* mice. Mean transit time (s) is visually observed to have no difference amongst groups. Following DCE-CT protocol, maps were generated using a Johnson-Wilson-Lee deconvolution model (n=4-5

mice/genotype). Red arrow points to ROI drawn in orange placed in the lower section of the myocardium captured. Care was taken to avoid placing the ROI too close to the left ventricle. *Mdx/Utrn*^{+/+} = *Mdx*, and *C57bl/10*=wild-type mice

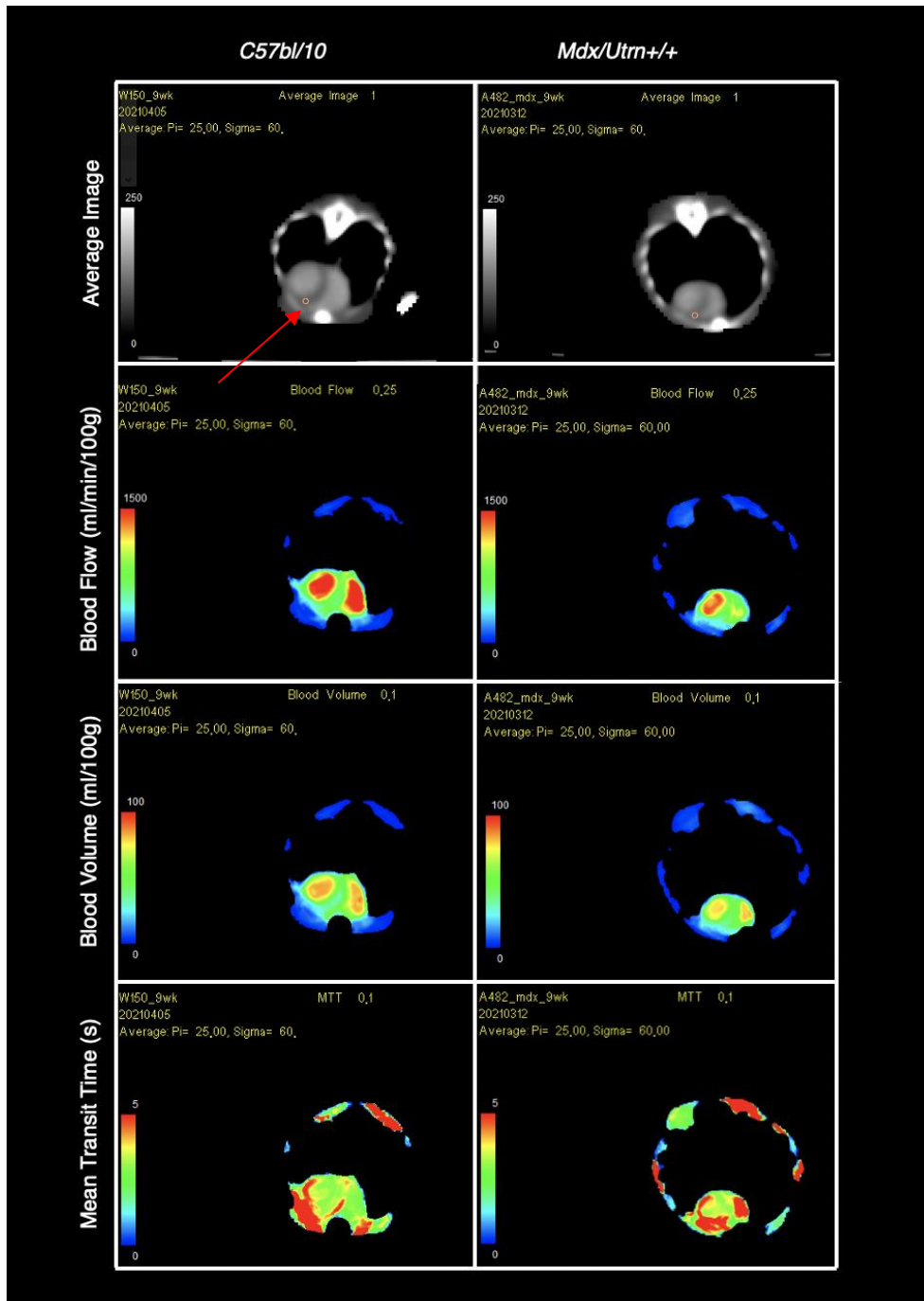


Figure 2.6 Comparison between *C57bl/10* and *mdx* cardiac regions with respect to blood flow (ml/min/100g), blood volume (ml/100g), and mean transit time (s) at the

8-10 week time point (n=1 biological and n=1 technical replicate per genotype group).

Mdx qualitatively depict increases in blood volume (ml/100g), and blood flow (ml/min/100g) within regions of the heart when compared to *C57bl/10* mice. Mean transit time (s) is visually observed to decrease amongst groups. Following DCE-CT protocol, maps were generated using a Johnson-Wilson-Lee deconvolution model (n=3 mice/genotype). Red arrow points to ROI drawn in orange placed in the lower section of the myocardium captured. Care was taken to avoid placing the ROI too close to the left ventricle. *Mdx/Utrn*^{+/+} = *Mdx*, and *C57bl/10*=wild-type mice

2.3.4 Differences in hemodynamic parameters are deemed not statistically significant at both 4-5 week and 8-10 week time points in DMD hindlimb regions

Mdx mice qualitatively depict similar BV, BF, and MTT within hind limb regions when compared to *C57bl/10* mice at both the 4-5 week time point (Figure 2.7) and 8-10 week time point (Figure 2.8).

Upon ROI perfusion calculation while BV, BF, and MTT increased, these findings did not reach significance. Specifically, BF increased by 12.30% (p=0.37), BV increased by 15.42% (p=0.26), and MTT increased by 3.89% (p=0.87) when compared between *mdx* and *C57bl/10* groups at 4-5 weeks (Figures 2.9, 2.11, and 2.13).

Notably at 8-10 weeks, BV, and MTT increased by 10.61% (p=0.62) and 14.95% (p=0.57). However, a difference in trends was observed from the prior time point. At this time point BF was noted to decrease by 3.45% (p=0.83) (Figures 2.10, 2.12, and 2.14).

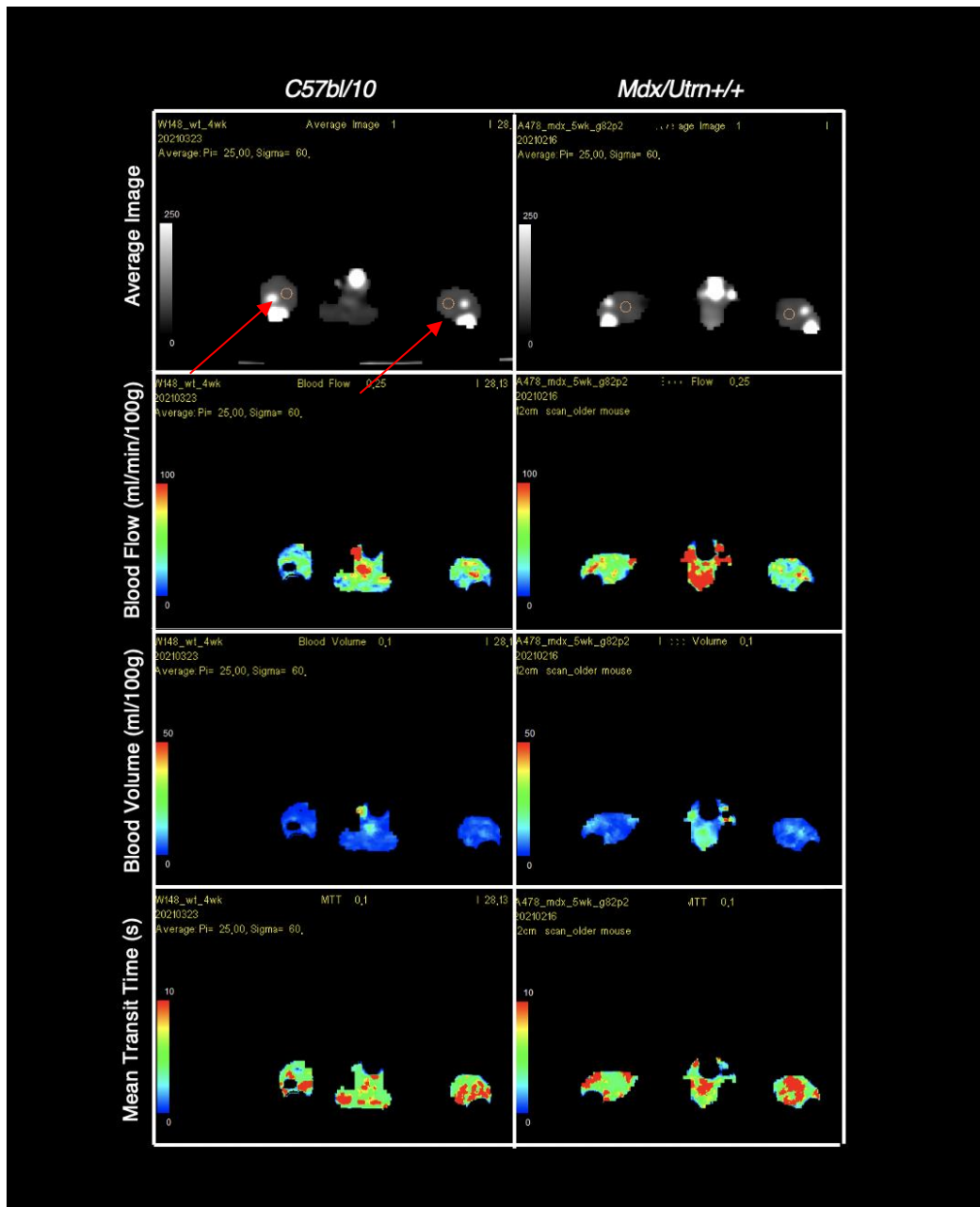


Figure 2.7 Comparison between *C57bl/10* and *mdx* hind limb regions with respect to blood flow (ml/min/100g), blood volume (ml/100g), and mean transit time (s) at the 4-5 week time point (n=1 biological and n=1 technical replicate per genotype group). *Mdx* qualitatively depicts increases in blood volume (ml/100g), blood flow (ml/min/100g), and mean transit time (s) within hindlimb regions when compared to *C57bl/10* mice. Following DCE-CT protocol, maps were generated using a Johnson-Wilson-Lee deconvolution model (n=4-5 mice/genotype). Red arrow points to ROI drawn in orange

placed in the widest section of each leg captured, and later averaged. Care was taken to avoid placing the ROI too close to tibia and fibula regions. *Mdx/Utrn*^{+/+} = *Mdx*, and *C57bl/10*=wild-type mice

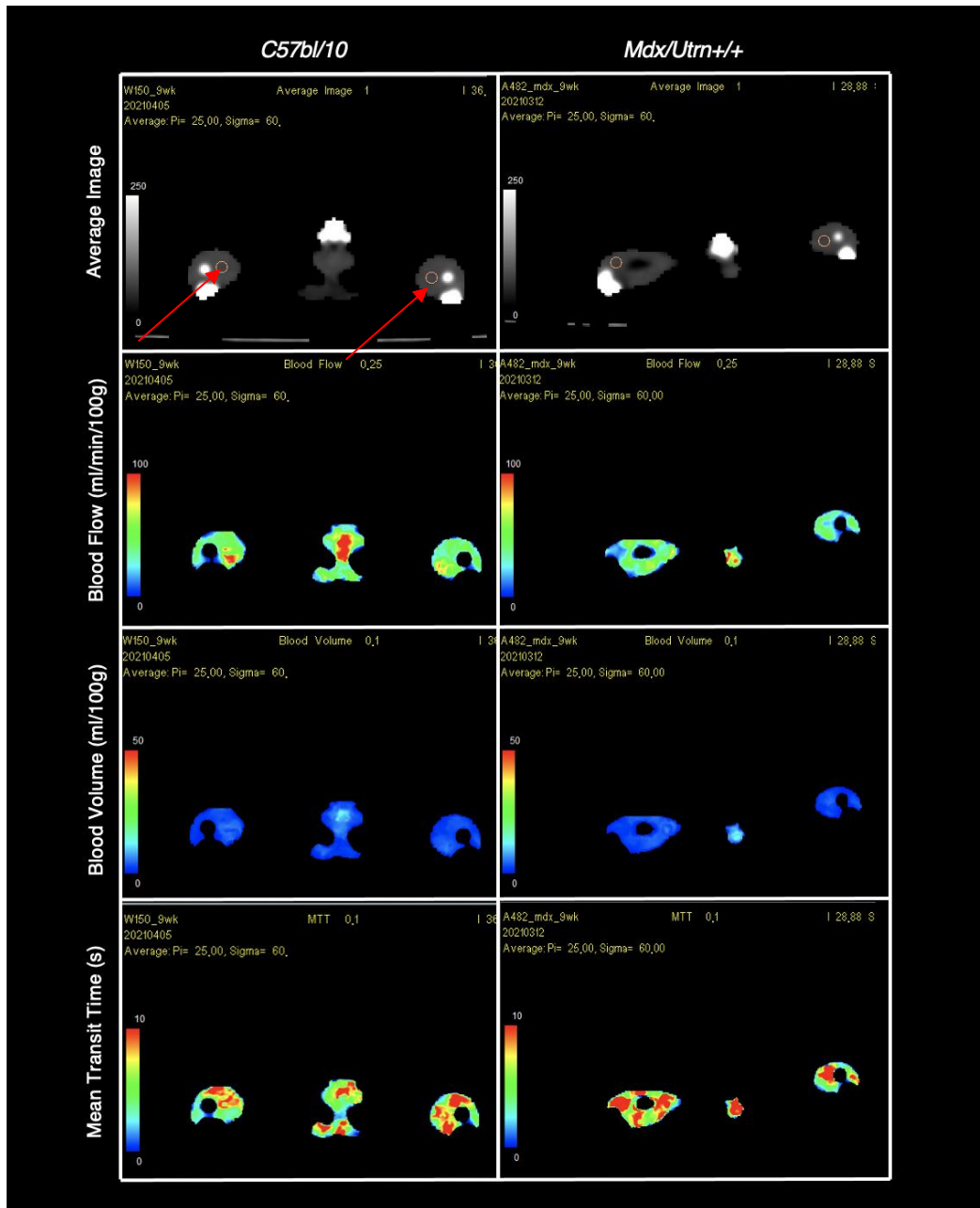


Figure 2.8 Comparison between *C57bl/10* and *mdx* hind limb regions with respect to blood flow (ml/min/100g), blood volume (ml/100g), and mean transit time (s) at the 8-10 week time point (n=1 biological and n=1 technical replicate per genotype group).

Mdx qualitatively depict increases in blood volume (ml/100g), blood flow (ml/min/100g), and mean transit time (s) within hindlimb regions when compared to *C57bl/10* mice. Following DCE-CT protocol, maps were generated using a Johnson-Wilson-Lee deconvolution model (n=3 mice/genotype). Red arrow points to ROI drawn in orange placed in the widest section of each leg captured, and later averaged. Care was taken to avoid placing the ROI too close to tibia and fibula regions. *Mdx/Utrn*^{+/+} = *Mdx*, and *C57bl/10*=wild-type mice

2.3.5 Comparison of blood flow at the 4-5 week and 8-10 week time points

Following comparison of site specific BF, BV, and MTT parameters, an overview of body-wide blood flow comparison was compiled (Figure 2.9). Here, we see that the biggest change with respect to blood flow occurs in the brain at the 4-5 week time point; an increase of 17.00% (p=0.14). The second largest change in blood flow occurs at the same time point in the hind limb region; an increase by 12.30% (p=0.37) when comparing *mdx* and *C57bl/10* groups. Between the 4-5 week time point and 8-10 week time point we see opposite trends pertaining to changes in blood flow in the brain and hindlimb areas. In the brain an overall decrease in BF from the prior increase of 17.00% (p=0.14) at the early time point to a 11.11% decrease (p=0.68) at the later time point is noted. In addition, within hindlimb regions we see that BF perfusion changes from a 12.30% (p=0.37) increase into an overall decrease of 3.45% (p=0.83) between *mdx* and control group mice (Figure 2.9).

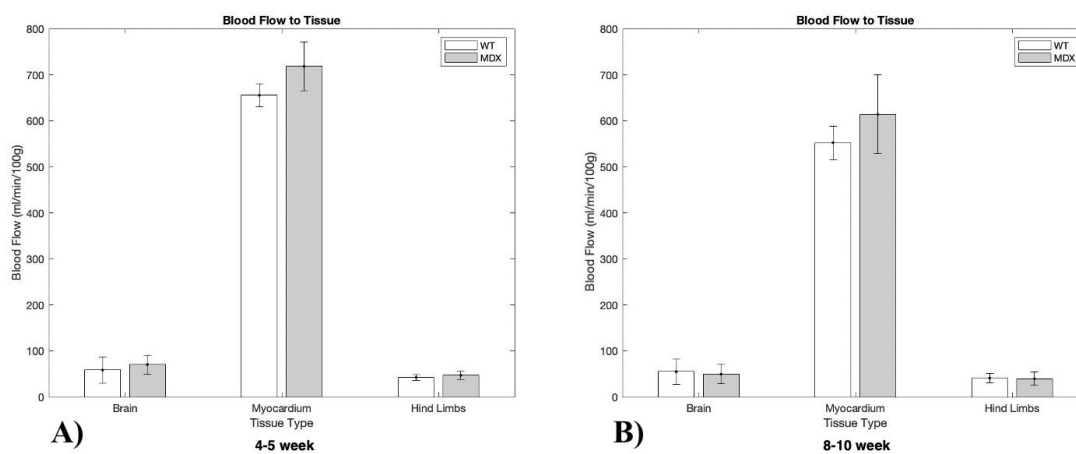


Figure 2.9 Comparison of blood flow to brain, myocardium and hind limbs at the A) 4-5 week time point between *mdx* (n=5) and *C57bl/10* mice (n=4) and B) 8-10 week time point between *mdx* (n=3) and *C57bl/10* mice (n=3).

Blood flow values for both time points were generated from arterial enhancement curves, and quantified using ROI segmentation within the brain, myocardium, and hind limbs (n=3-5 mice/genotype). Although results did not reach significance, notable trends are observed between the two time points for both *C57bl/10* mice (white bars) and *mdx* mice (gray bars). Welch's two-way t-test was used to determine significance. Data is depicted as mean \pm SD.

2.3.6 Comparison of blood volume at the 4-5 week and 8-10 week time points

Next, an overview of body-wide blood volume comparison was compiled (Figure 2.10). Here, we see that the biggest change with respect to blood volume occurs in the brain at the 8-10 week time point; a decrease of 29.29% (p=0.45). The second largest change in blood volume occurs at the same time point in the hind limb region; a decrease by 20.31% (p=0.62) when comparing *mdx* and *C57bl/10* groups. Between the 4-5 week time point and 8-10 week time point we see opposite trends pertaining to changes in blood volume in the brain and myocardium regions. In the brain an increase of 16.06% (p=0.13) at the early time point shifts to a decrease by 29.29% (p=0.68) at the later time point. In addition, within myocardium regions we see that BV perfusion changes from a 9.47% (p=0.22) increase at the early pre-fibrotic time point into an overall decrease of 20.31% (p=0.32) between *mdx* and control group mice at the later fibrotic time point (Figure 2.10).

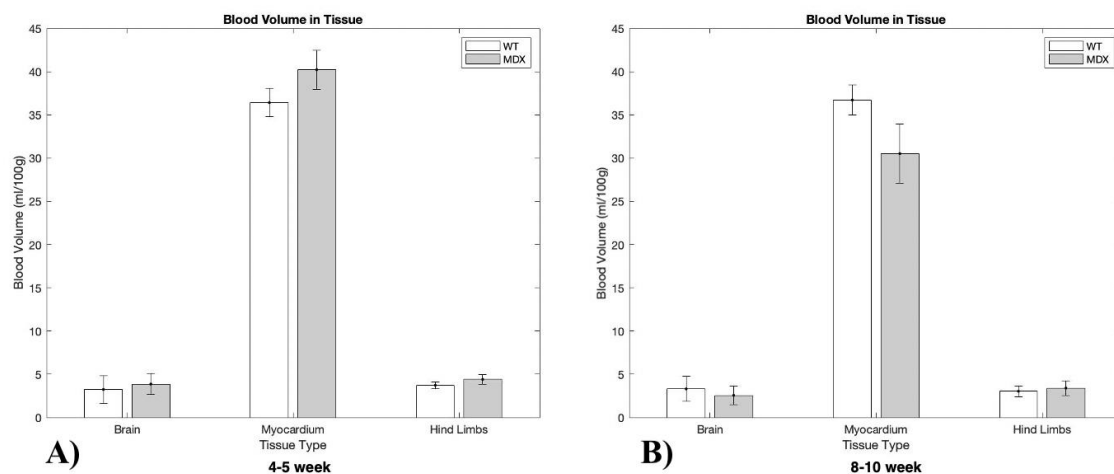


Figure 2.10 Comparison of blood volume to brain, myocardium and hind limbs at the A) 4-5 week time point between *mdx* (n=5) and *C57bl/10* mice (n=4) and the B) 8-10 week time point between *mdx* (n=3) and *C57bl/10* mice (n=3).

Blood volume values were generated from arterial enhancement curves, and quantified using ROI segmentation within the brain, myocardium, and hind limbs (n=3-5 mice/genotype) at both time points. Although results did not reach significance, notable trends are observed between the two time points for *C57bl/10* mice (white bars) and *mdx* mice (gray bars). Welch's two-way t-test was used to determine significance. Data is depicted as mean \pm SD.

2.3.7 Comparison of mean transit time at the 4-5 week and 8-10 week time points

Following the comparison of systemic BV trends an overview of body-wide MTT comparison was compiled (Figure 2.11). Here, we see that the biggest change with respect to MTT occurs in brain the at the 8-10 week time point; a decrease of 55.90% (p=0.24). The second largest change in MTT occurs at the same time point in the myocardium region; a decrease by 16.67% (p=0.32) when comparing *mdx* and *C57bl/10* groups. Between the 4-5 week time point and 8-10 week time point the same trend in MTT is observed across all three regions. We see increases in MTT in the brain and heart across these two time points, and a continuing decrease in MTT in the hindlimbs (Figure 2.11).

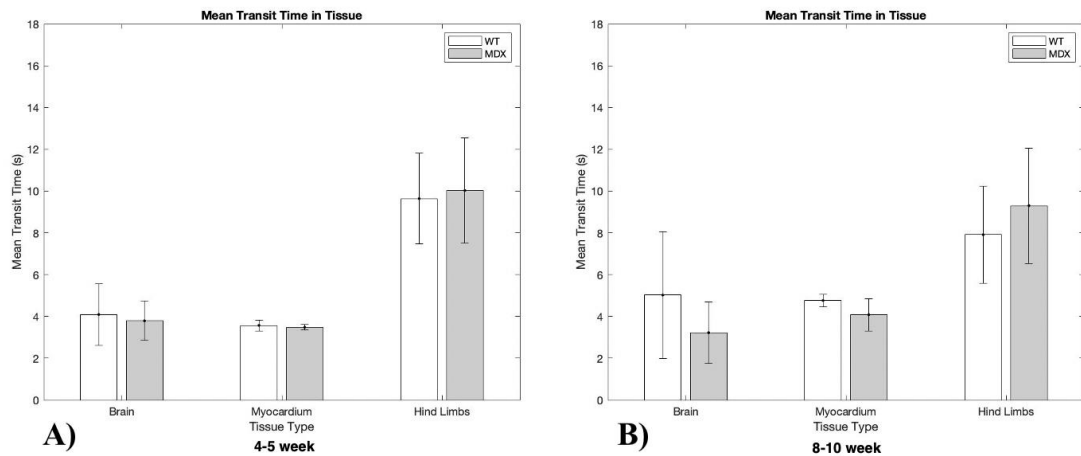


Figure 2.11 Comparison of mean transit time to brain, myocardium and hind limbs at the A) 4-5 week time point between *mdx* (n=5) and *C57bl/10* mice (n=4) and at the B) 8-10 week time point between *mdx* (n=3) and *C57bl/10* mice (n=3)..

Mean transit time values were generated from arterial enhancement curves, and quantified using ROI segmentation within the brain, myocardium, and hind limbs (n=3-5 mice/genotype) for both time points. Although results did not reach significance, notable trends are observed between both time points for *C57bl/10* mice (white bars) and *mdx* mice (gray bars). Welch's two-way t-test was used to determine significance. Data is depicted as mean \pm SD.

A)

<i>C57bl/10</i> 4-5 weeks						
	Blood Flow	SD	Blood Volume	SD	Mean Transit Time	SD
Brain	58.49	28.62	3.24	1.62	4.09	1.48
Myocardium	655.32	25.23	36.41	1.65	3.57	0.26
Hindlimbs	42.42	6.54	3.73	0.40	9.64	2.17
<i>Mdx</i> 4-5 weeks						

	Blood Flow	SD	Blood Volume	SD	Mean Transit Time	SD
Brain	70.47	20.52	3.86	1.20	3.79	0.95
Myocardium	718.25	52.59	40.22	2.28	3.48	0.14
Hindlimbs	46.99	9.04	4.41	0.56	10.03	2.52

B)

<i>C57bl/10 8-10 weeks</i>						
	Blood Flow	SD	Blood Volume	SD	Mean Transit Time	SD
Brain	54.98	27.54	3.31	1.42	5.02	3.03
Myocardium	552.28	36.17	36.72	1.73	4.76	0.31
Hindlimbs	41.05	9.55	3.03	0.60	7.91	2.33
<i>Mdx 8-10 weeks</i>						
	Blood Flow	SD	Blood Volume	SD	Mean Transit Time	SD
Brain	49.48	20.71	2.56	1.07	3.22	1.48
Myocardium	613.88	85.91	30.52	3.39	4.08	0.78
Hindlimbs	39.68	14.33	3.40	0.85	9.30	2.76

Table 1. Quantitative values for Blood flow (ml/min/100g), Blood Volume (ml/100g), and Mean Transit Time (s) at A) the 4-5 week time point and B) 8-10 week time point between *C57bl/10* and *mdx* mice.

2.3.8 *Ex-vivo* MPO signal is significantly heightened at the pre-fibrotic time point of 4-5 weeks in DMD brain tissue

Following the collection of DCE-CT data, *ex-vivo* histology was analyzed to test the hypothesis if oxidative stress is correlated with hemodynamic parameters. At the early time point, 4-5 weeks, DMD mice exhibit significant increases in MPO signal. This is noted by a 13.78% ($p=0.01$) increase in MPO deposition in DMD neural tissue (Figure 2.14, Figure 2.15). Within skeletal muscle ($p=0.99$) and cardiac tissue ($p=0.11$) MPO deposition is deemed not statistically significant (Figure 2.19, Figure 2.23). Interestingly, within cardiac tissue results had notable trends. Within cardiac tissue MPO deposition is seen to increase by 16.99% ($p=0.11$) (Figure 2.19). These results coincide with findings pertaining to H&E and MT staining in the heart and skeletal muscle, as no visible hallmarks of fibrosis or collagen deposition were observed (Figures 2.16, 2.17, 2.20, and 2.21).

2.3.9 MPO Signal is significantly heightened at the fibrotic time point of 8-10 weeks in DMD heart and skeletal tissue

Following the collection of *ex-vivo* histology at the 4-5 week time point, histology pertaining to the 8-10 week time point was analyzed across the brain, heart, and skeletal muscle. At this time point, 8-10 weeks, DMD mice exhibit significant increases in MPO signal within the heart and skeletal tissue. This is noted by a 14.53% ($p=0.03$) increase in MPO deposition in DMD cardiac tissue, and a 15.70% ($p=0.0006$) increase in skeletal tissue (Figure 2.19, Figure 2.23). Within neural tissue at this time point, MPO deposition is deemed not statistically significant ($p=0.19$) (Figure 2.15). These results coincide with findings pertaining to H&E and MT staining in the heart and skeletal muscle, as early stages of fibrosis and collagen deposition were observed (Figures 2.16, 2.17, 2.20, and 2.21).

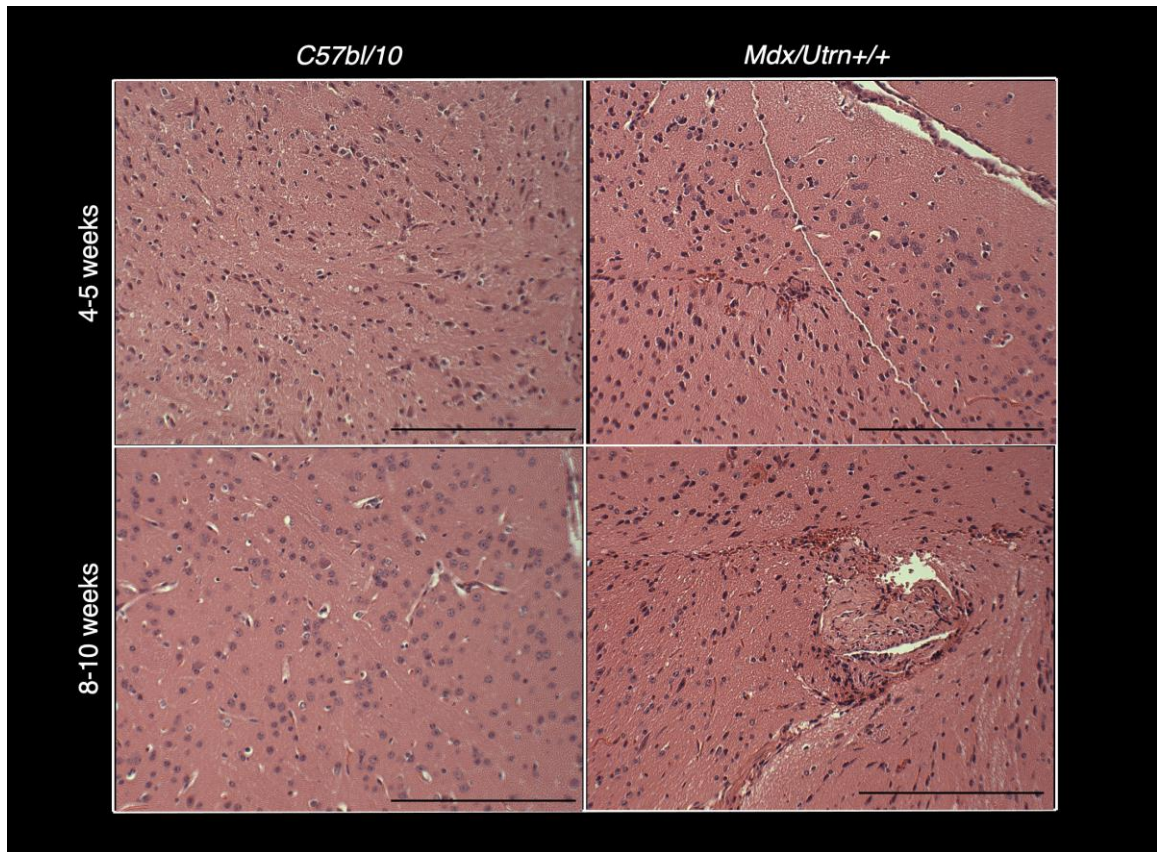


Figure 2.12 *mdx* mice at 4-5 weeks and 8-10 weeks exhibit infiltrate within brain tissue.

Brain tissue was obtained from *mdx* and *C57bl/10* mice at 4-5 week and 8-10 week old time points and then stained with hematoxylin and eosin (H&E) to view general histology of tissue (scale bar = 100 μ m); one biological and one technical replicate used.

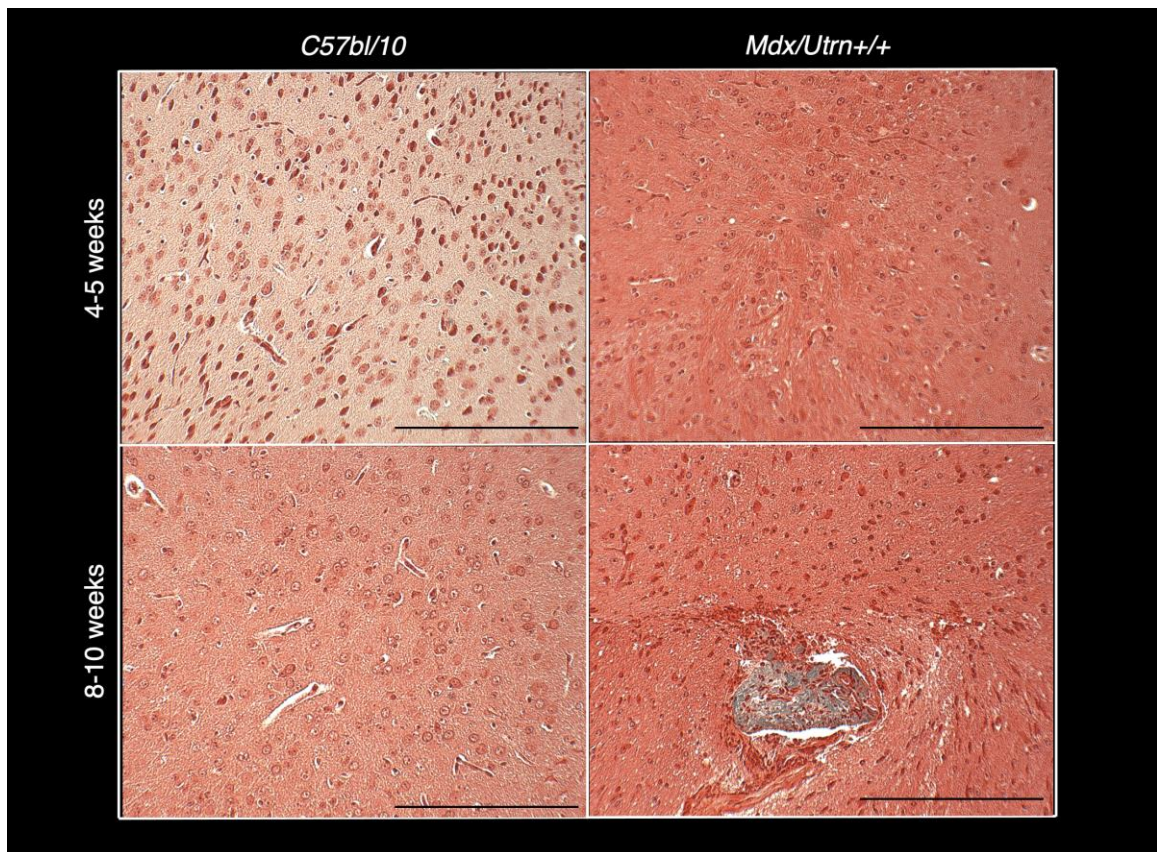


Figure 2.13 *Mdx* mice at 8-10 weeks exhibit collagen deposition within brain tissue.

Brain tissue was obtained from *mdx* and *C57bl/10* mice at 4-5 week and 8-10 week old time points and then stained with Masson's Trichrome to differentiate collagen deposition (blue), from muscle, fibrin, and cytoplasm (red), and nuclei (dark red) in tissue (scale bar = 100 μ m); one biological and one technical replicate used.

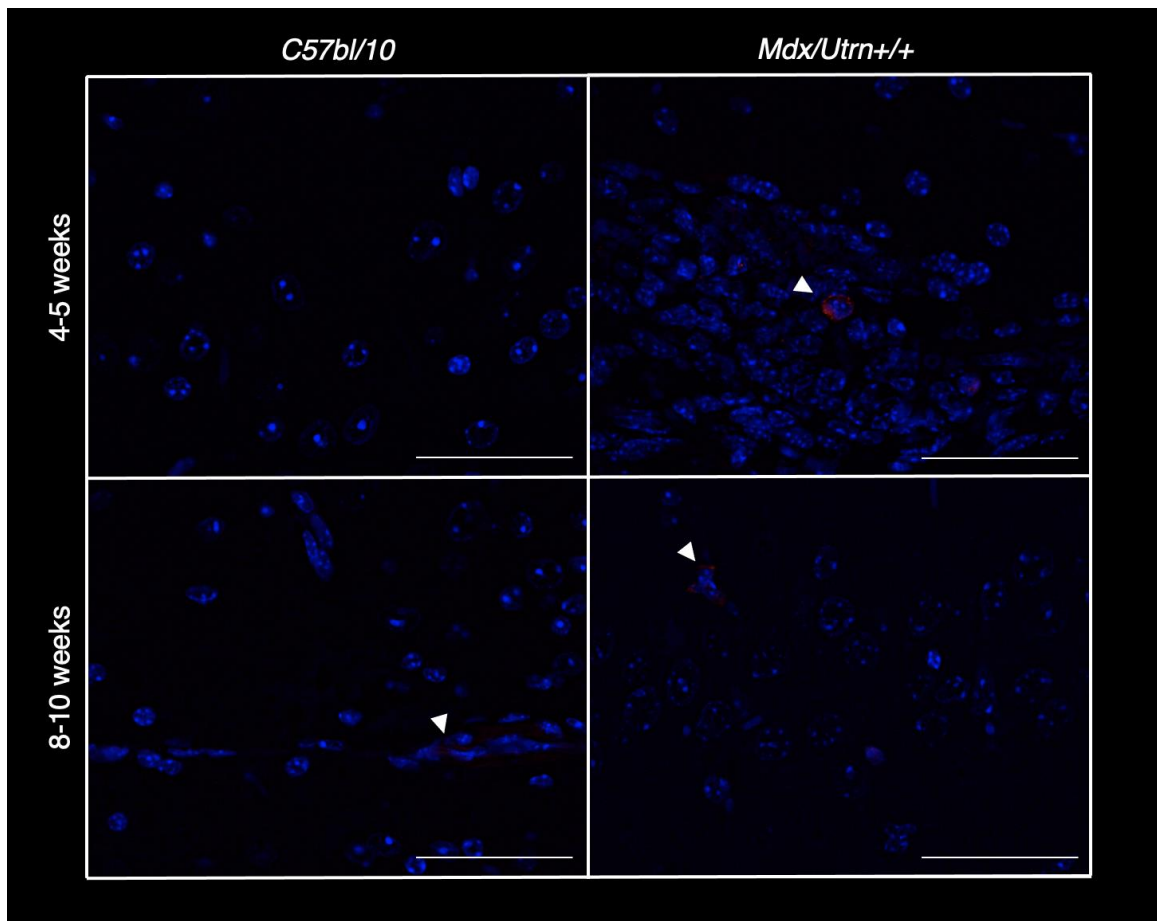


Figure 2.14 Comparison of *mdx* mice to *C57bl/10* at 4-5 weeks and 8-10 weeks, with respect to MPO deposition in neural tissue, exhibits significantly higher signal in *mdx* at the 4-5 week time point than 8-10 week time point when compared to the *C57bl/10* group

Brain tissue was obtained from *mdx* and *C57bl/10* mice at 4-5 week and 8-10 week old time points and then stained with MPO (red), and DAPI (blue). White arrow heads point towards MPO signal (scale bar = 20 μm); three biological and three technical replicates used.

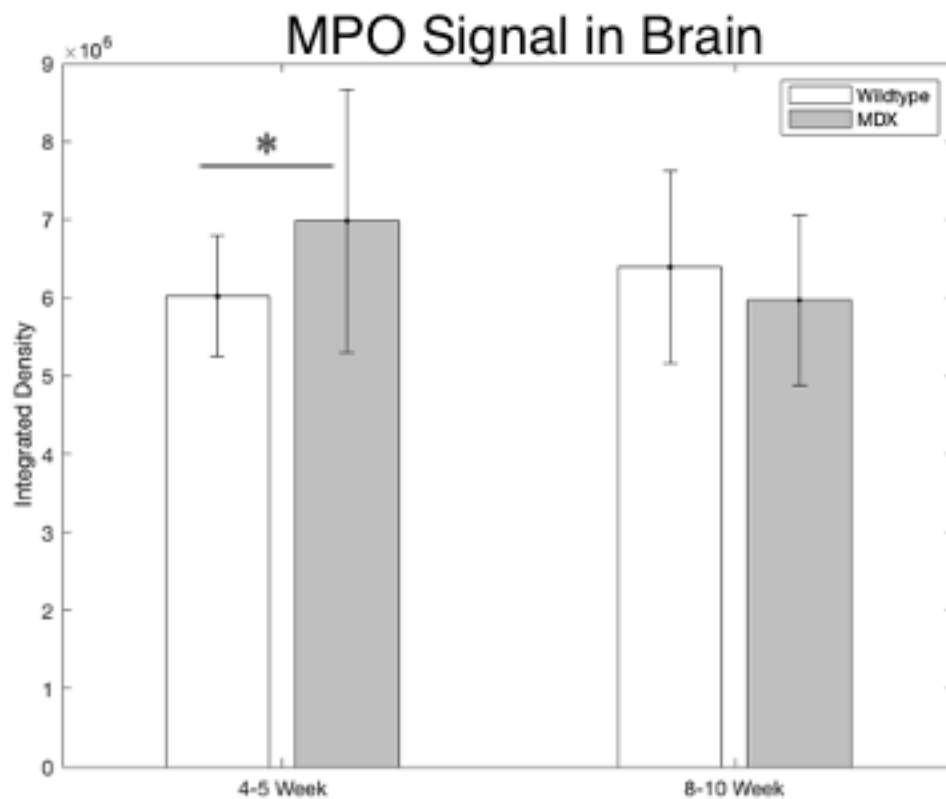


Figure 2.15 Quantified signal of MPO deposition in *mdx* mice at 4-5 weeks (p=0.01) and 8-10 weeks (p=0.19) compared to *C57bl/10* mice within brain tissue.

Brain tissue was obtained from *mdx* and *C57bl/10* mice at 4-5 week and 8-10 week old time points and then stained with MPO. Data displayed with mean \pm SD indicates that MPO signal is higher at the 4-5 week time point than 8-10 week time point in *Mdx* mice. Three biological and three technical replicates were used; 9 images per biological replicate were used to quantify signal. *

2.3.10 *Ex-vivo* MPO signal is significantly heightened at the fibrotic time point of 8-10 weeks in DMD cardiac tissue

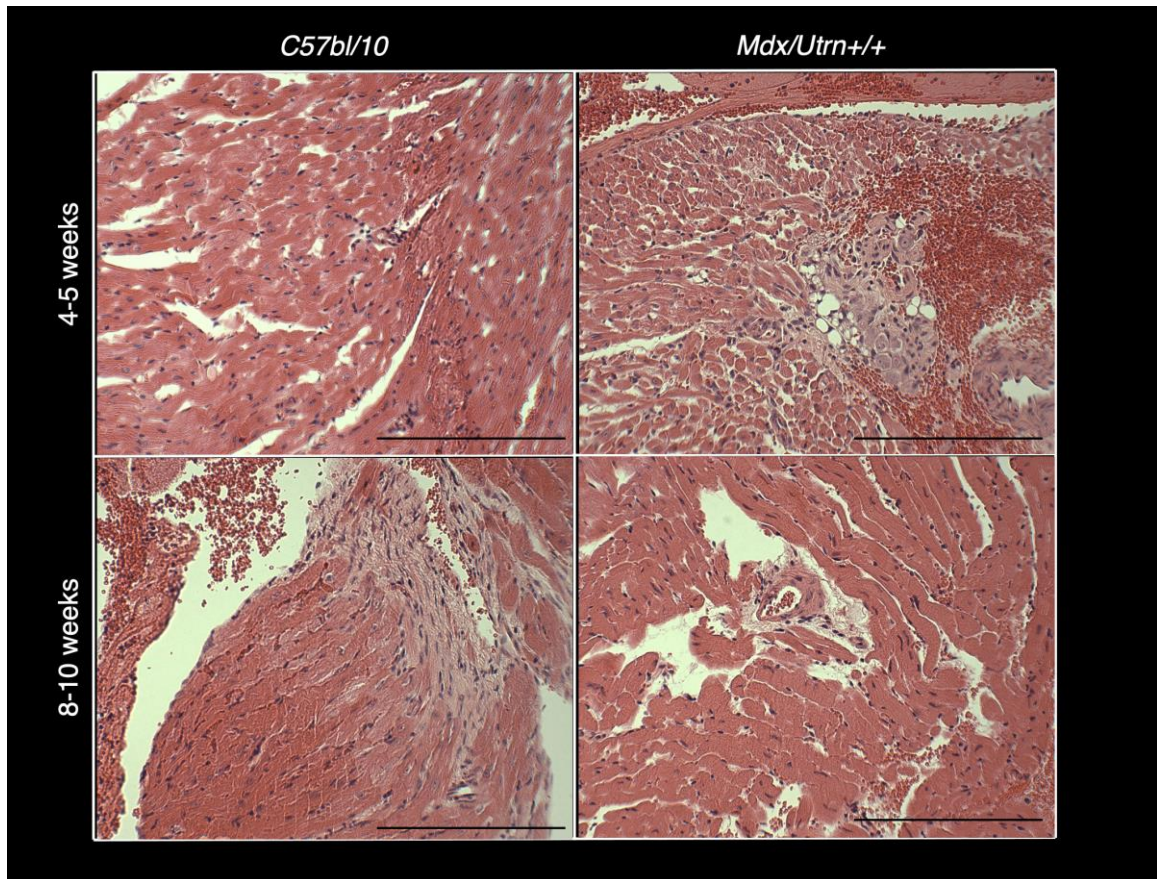


Figure 2.16 *Mdx* mice at 4-5 weeks and 8-10 weeks exhibit mild cases of centric nuclei within cardiac tissue when compared to *C57bl/10* mice.

Cardiac tissue was obtained from *mdx* and *C57bl/10* mice at 4-5 week and 8-10 week old time points and then stained with H&E to differentiate disease pathology in tissue (scale bar = 100 μ m); one biological and one technical replicate used.

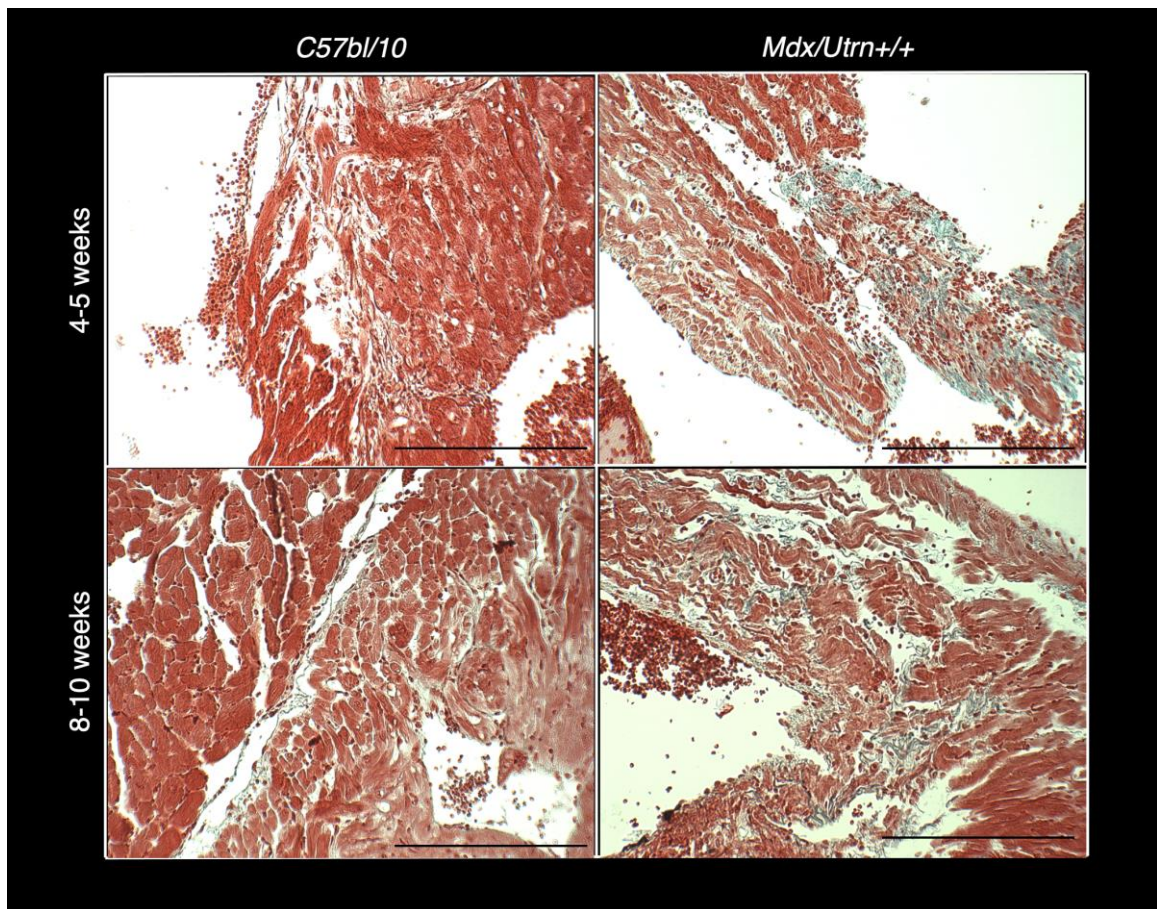


Figure 2.17 *Mdx* mice at 4-5 weeks and 8-10 weeks exhibit collagen deposition within cardiac tissue when compared to *C57bl/10* mice.

Cardiac tissue was obtained from *mdx* and *C57bl/10* mice at 4-5 week and 8-10 week old time points and then stained with Masson's Trichrome to differentiate collagen deposition (blue), from muscle, fibrin, and cytoplasm (red), and nuclei (dark red) in tissue (scale bar = 100 μ m); one biological and one technical replicate used.

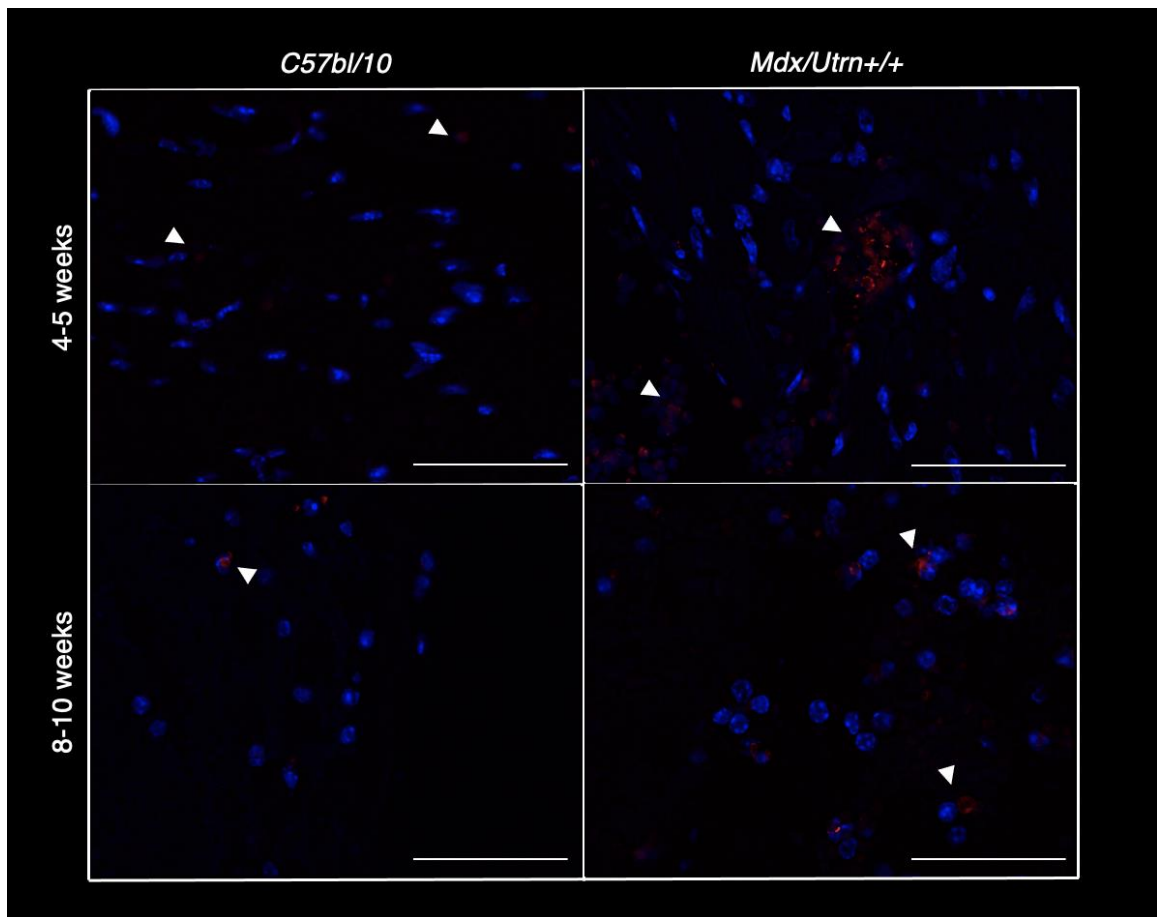


Figure 2.18 Comparison of *mdx* mice to *C57bl/10* at 4-5 weeks and 8-10 weeks with respect to MPO deposition in cardiac tissue, exhibits significantly higher MPO deposition at both time points in *mdx* group when compared to *C57bl/10* group

Cardiac tissue was obtained from *mdx* and *C57bl/10* mice at 4-5 week and 8-10 week old time points and then stained with MPO (red), and DAPI (blue). White arrow heads point towards MPO signal (scale bar = 20 μm); three biological and three technical replicates used.

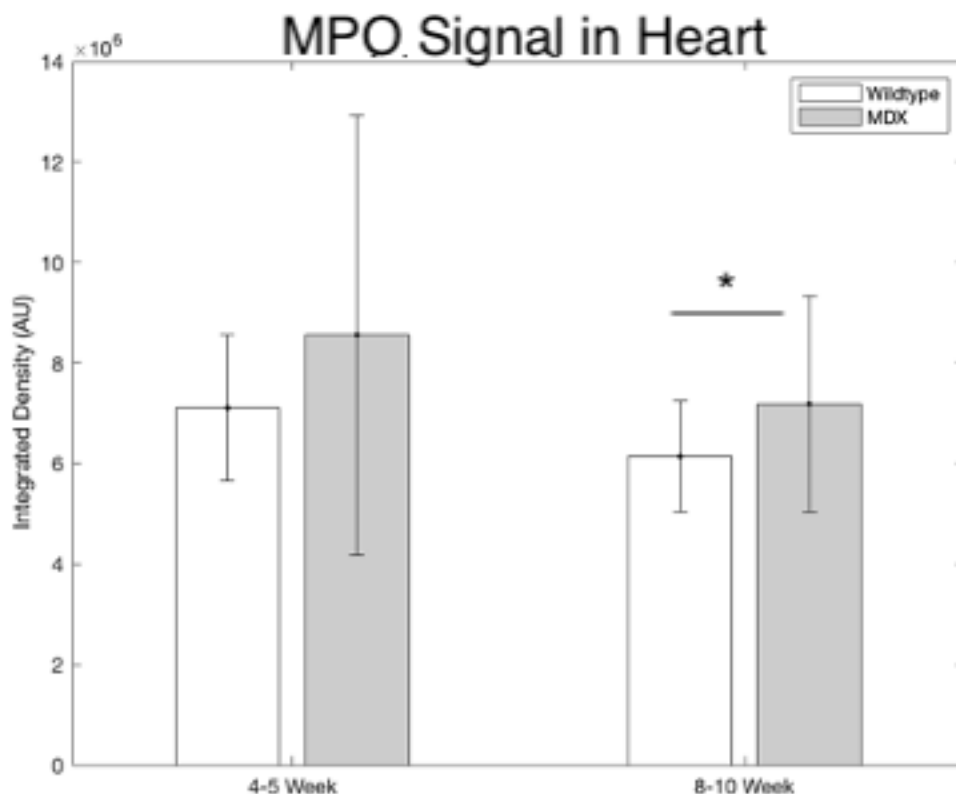


Figure 2.19 Quantified signal of MPO deposition in *mdx* mice at 4-5 weeks ($p=0.11$) and 8-10 weeks ($p=0.03$) compared to *C57bl/10* mice exhibited within cardiac tissue.

Cardiac tissues were obtained from *mdx* and *C57bl/10* mice at 4-5 week and 8-10 week old time points and then stained with myeloperoxidase. Data displayed with mean \pm SD, indicate that there is a significant increase in MPO signal at the 8-10 week time point ($p=0.03$) between the *mdx* and *C57bl/10* group. Three biological and three technical replicates were used; 9 images per biological replicate were used to quantify signal.

2.3.11 *Ex-vivo* MPO signal is significantly heightened at the fibrotic time point of 8-10 weeks in DMD skeletal muscle tissue

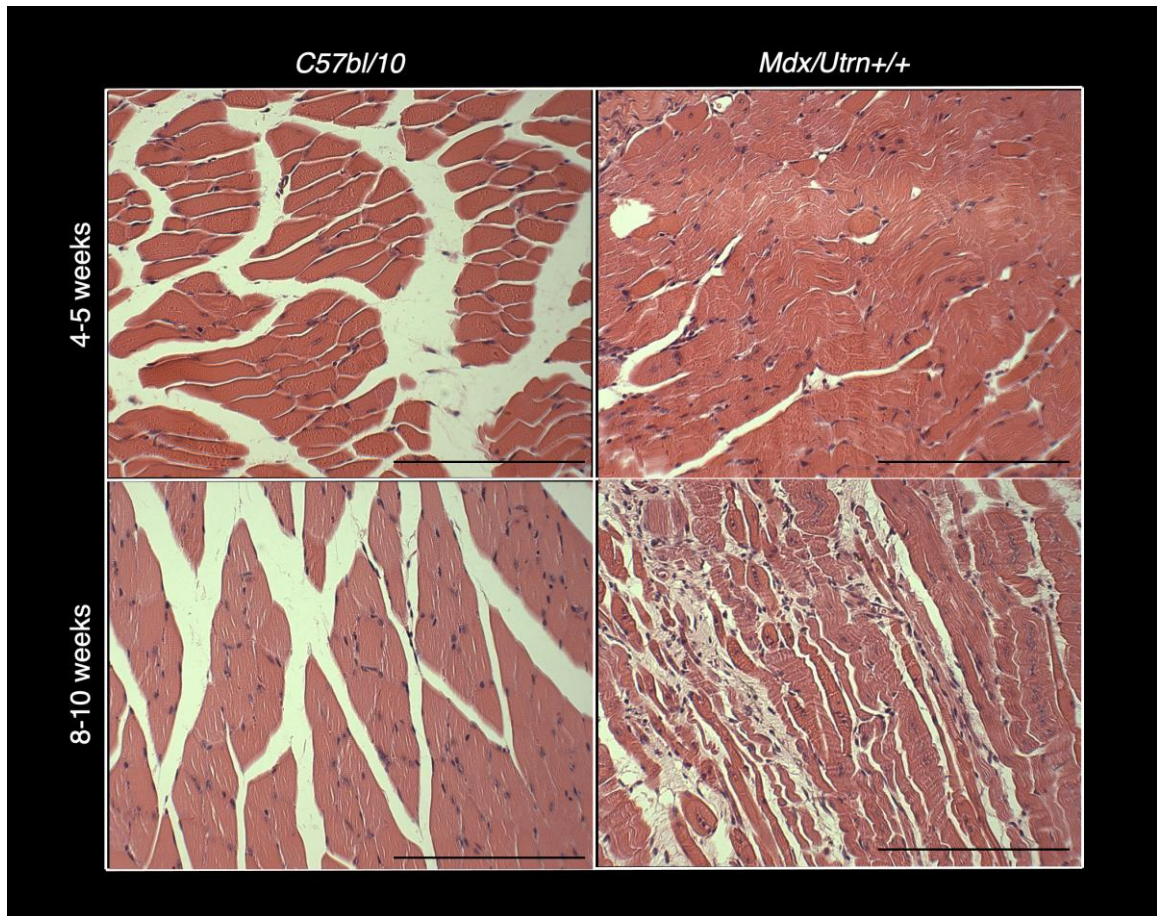


Figure 2.20 *Mdx* mice at 4-5 weeks and 8-10 weeks exhibit centric nuclei within gastrocnemius muscle when compared to *C57bl/10* mice.

Gastrocnemius muscle was obtained from *mdx* and *C57bl/10* mice at 4-5 week and 8-10 week old time points and then stained with H&E to differentiate disease pathology in tissue (scale bar = 100 μ m); one biological and one technical replicate used.

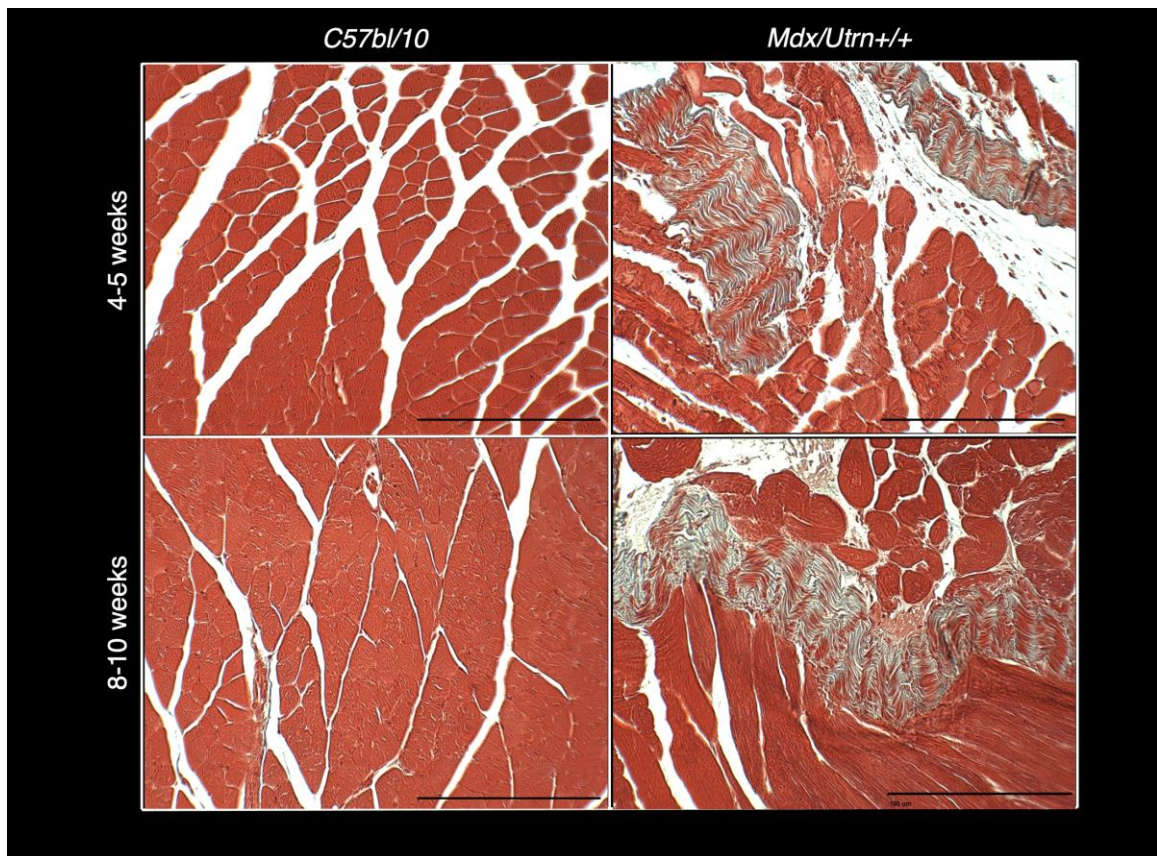


Figure 2.21 *Mdx* mice at 4-5 weeks and 8-10 weeks exhibit collagen deposition within gastrocnemius muscle when compared to *C57bl/10* mice.

Gastrocnemius muscle was obtained from *mdx* and *C57bl/10* mice at 4-5 week and 8-10 week old time points and then stained with Masson's Trichrome to differentiate collagen deposition (blue), from muscle, fibrin, and cytoplasm (red), and nuclei (dark red) in tissue (scale bar = 100 μm); one biological and one technical replicate used.

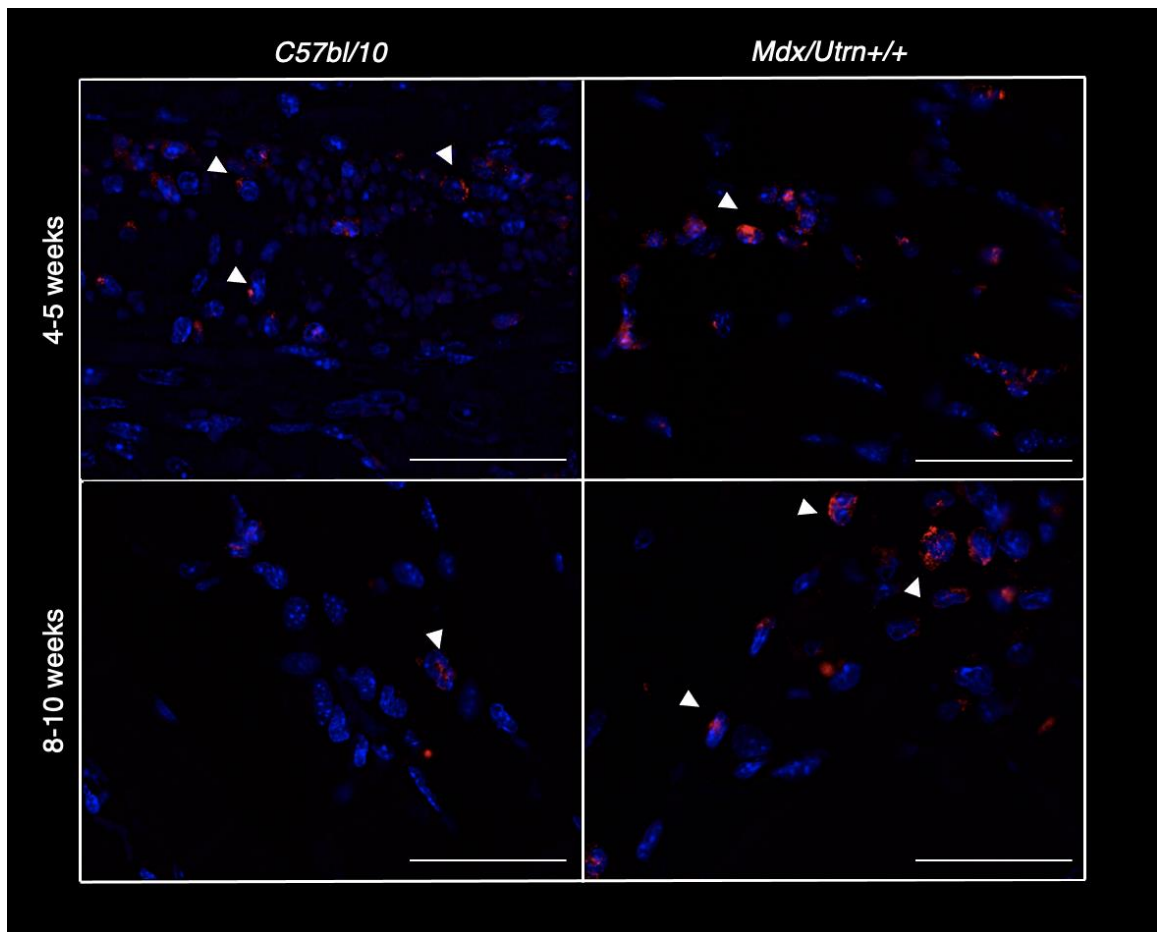


Figure 2.22 Comparison of *mdx* mice to *C57bl/10* at 4-5 weeks and 8-10 weeks with respect to MPO deposition in gastrocnemius tissue, exhibit significantly higher MPO deposition at the 8-10 week time point in *mdx* group when compared to *C57bl/10* group

Gastrocnemius tissue was obtained from *mdx* and *C57bl/10* mice at 4-5 week and 8-10 week old time points and then stained with MPO (red), and DAPI (blue). White arrow heads point towards MPO signal (scale bar = 20 μm); three biological and three technical replicates used.

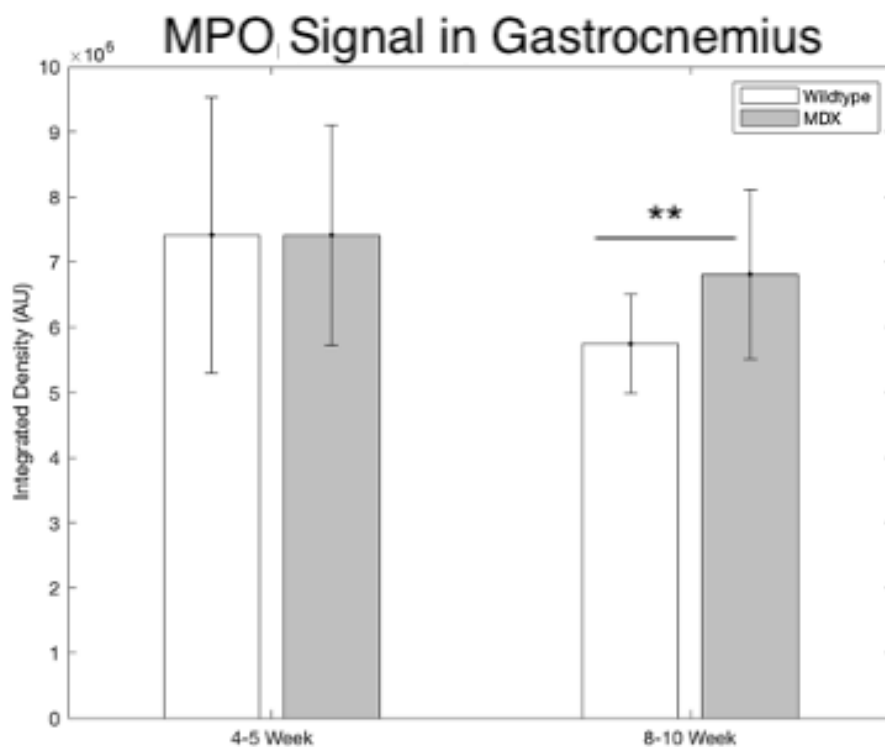


Figure 2.23 Quantified signal of MPO deposition in *mdx* mice at 4-5 weeks ($p=0.99$) and 8-10 weeks ($p=0.006$) compared to *C57bl/10* mice within gastrocnemius muscle.

Gastrocnemius muscle was obtained from *mdx* and *C57bl/10* mice at 4-5 week and 8-10 week old time points and then stained with MPO. Data displayed with mean \pm SD indicate that there is a significant difference in MPO signal at the 8-10 week time point. Three biological and three technical replicates were used; 9 images per biological replicate were used to quantify signal.

2.4 Discussion

Chronic inflammation is a hallmark of DMD pathophysiology. H&E staining qualitatively depicted infiltration within the brain at the 4-5 week time point and 8-10 week time point whereas Masson's trichrome depicted collagen deposition beginning at the 8 to 10 week time point (Figure 2.12, Figure 2.13). In our investigation, MPO signal deposition was highest at the 4 to 5 week time point ($p=0.01$) in the brain (Figure 2.15). Moreover, we may infer that this may indicate that ROS accumulations precede collagen

deposition in neural tissue. Studies using MRI and spectroscopy have shown both metabolic and structural changes within the *mdx* murine model brain. When compared to the control group, *mdx* mice were shown to have enlarged lateral ventricles and elevated diffusion diffusivities in the prefrontal cortex, and reduced diffusivities within the hippocampus.¹⁵ Paired with this data, elevations in anti-oxidant species such as glutathione, phosphocholine, and reduced gamma-aminobutyric acid in the hippocampus were detected.¹⁶ Together these results indicate that there are structural changes within the brain and altered antioxidant defenses in DMD neural tissue¹⁶. Since the role of dystrophin within the brain is not well characterized, and mechanisms pertaining to pathology and etiology of DMD in this location remain elusive, our results may shed light on oxidative stress mechanisms within the brain at earlier time points in DMD. Specifically, the 4-5 week time point where MPO was found to be increased ($p=0.01$) in *mdx* groups when compared against the control group (Figure 2.14, Figure 2.15). MPO derived oxidants have been found to induce blood brain barrier dysfunction, as one study conducted in lipopolysaccharide-treated mice found that the barrier was rescued by MPO inhibitors 4-aminobenzoic acid hydrazide.¹⁷

Within cardiac tissue, mild cases infiltration was observed at both time points (Figure 2.16). Collagen deposition looked qualitatively larger with age/disease progression in *mdx* mice when compared to *C57bl/10* (Figure 2.17). MPO signal deposition was significantly larger at the 8 to 10 week time point ($p=0.03$) in DMD cardiac tissue (Figure 2.18, Figure 2.19). One may speculate that the functional pathology of DMD may be responsible for the data observed in our study. Mitochondrial-mediated cell death may be one pathway that contributes to cardiac dysfunction, as the conductivity of the heart is impaired thus leading to necrosis and inflammation¹⁸. As previously mentioned, the ECM is sensitive to inflammation-associated oxidants and recent studies have found that hypochlorous acid derived from MPO can modify certain ECM proteins resulting in decreased cell adhesion and creation of leakier vasculature which in turn creates a positive feedback loop and increased MPO recruitment¹⁹. This gives credence to our finding that with age MPO deposition within cardiac tissue increases in *mdx* models when compared to *C57bl/10* (Figure 2.19).

Likewise, within gastrocnemius muscle centric nuclei were visible at both time points along with collagen deposition (Figure 2.20, Figure 2.21). Similar to the findings in cardiac tissue, MPO signal was significantly different at the 8 to 10 week time point ($p=0.001$) in gastrocnemius muscle (Figure 2.22, Figure 2.23). Interestingly, a recent, a study quantified MPO enzyme activity using a detergent compatible protein assay. It was found that within gastrocnemius muscle *N*-acetylcysteine significantly differed compared to control group ($p<0.001$) and inversely correlated to MPO levels at later stages of disease.²⁰ Like our findings, this study showed that with increasing age, MPO deposition increases within skeletal muscle; most likely due to damage accumulated overtime based on contraction injury (Figure 2.23).

A recent investigation found that peroxidase enzymes stimulate the migration of fibroblastic cells and help secrete collagenous proteins within the ECM, as a direct result of their profibrogenic capacity.²¹ Within our study, we observed that MPO was upregulated in almost all sites when compared to control groups (Figures 2.15, 2.19, and 2.23). This may be one of the reasons why we see an overall increase in collagen deposition within the *mdx* murine model when compared to the *C57bl/10* control group (Figures 2.13, 2.17, and 2.21).

However, it is important to note that between the two time points at all sites in the *mdx* mouse model, it was found that MPO expression decreases between the 4-5 week time point and 8-10 week time point (Figures 2.15, 2.19, and 2.23). One explanation to this trend, may be the activation of utrophin within the murine *mdx* model, which occurs around 8-10 weeks of age. Utrophin has been shown to revert certain markers of oxidative stress, and markers of protein oxidation, so much so as to bring the levels to baseline levels similar to those found in control groups. Precisely one research group found that increased levels of utrophin expression was responsible for ameliorating the effects of mitochondrial dysfunction as seen in *mdx* and double knock out murine models of DMD.²²

Arterial time enhancement curves at the four to five week time point displayed the peak of the *mdx* curve approximately 16 seconds delayed when compared to wild type mice.

At the eight to ten week age the time to peak was similar among both groups, approximately, 60 seconds, however the curve for *mdx* mice displayed a more gradual increase in arterial output over time when compared to control group (Figure 2.1, Figure 2.2). The shift in arterial curve between the two time points could have other mechanisms at play to cause such an effect. One hypothesis may be that the improvement of time to peak at the 8-10 week time point is due to utrophin expression, and as a result down regulation of oxidative species which in turn may correct vasculature dysfunction.

Despite the CT perfusion study not finding significant differences in hemodynamic parameters, there were notable trends within the data. In brain, there is an increase by 17.00% in blood flow ($p=0.14$), 16.06% increase in blood volume ($p=0.13$), and 7.92% decrease in mean transit time ($p=0.34$) at the 4-5 week time point (Figures 2.9A, 2.10A, and 2.11A). At the 8-10 week time point blood flow decreases by 11.11% ($p=0.68$), blood volume decreases by 29.29% ($p=0.45$), and mean transit time decreases by 55.90% ($p=0.24$) in brain (Figures 2.9B, 2.10B, and 2.11B). Reports in literature coincide with these findings as, one such study used arterial spin labeling and diffusion-weighted MRI on 2-month-old mice and showed that the leaky blood brain barrier was responsible for increased cerebral edema in the extracellular space which contributed to increased intracranial pressure. Similarly here, we see that there is increased blood volume and blood flow at the 4-5 week time point which may correspond to the accumulation of fluid within the brain.²³

This is in contrast to the 8-10 week time point, where we see overall decreases in perfusion (Figures 2.9B, 2.10B, and 2.11B). One may speculate given our H&E and Masson's Trichrome stained images that the accumulation of infiltrate, collagen, and fibrofatty deposits may be responsible for this phenotype and may even be due to impaired angiogenesis (Figures 2.12, 2.13, 2.16, 2.17, 2.20, and 2.21). Podkalicka et. Al, found that within male *mdx* mice angiogenesis at the 12 month time point was greatly reduced which was associated with decreased VEGF levels.²⁴ It is possible that angiogenesis within the brain when coupled with leaky vasculature may lead to further complications in neural tissue and may even be causative of cognitive defects as observed in patients.²⁵ One of the first MRI cerebral perfusion studies in DMD showed globally

reduced perfusion in DMD patients by roughly 17% when compared to the control population between ages of 8 to 18 years. The reduction in blood flow was found to be greatest in those lacking Dp140, which was associated with a reduction in grey matter.²⁶

Within cardiac tissue blood flow increases by 8.76% ($p=0.29$), blood volume increases by 9.47% ($p=0.22$), and mean transit time decreases by 2.59% ($p=0.78$) at 4-5 week time point (Figures 2.9A, 2.10A, and 2.11A). At the 8-10 week time point blood flow increases by 10.03% ($p=0.49$), blood volume decreases by 20.31% ($p=0.32$), and mean transit time decreases by 16.67% ($p=0.32$) (Figures 2.9B, 2.10B, and 2.11B). While the trend demonstrates that blood flow is increased at a similar percentage at both time points, the decrease in blood volume may be indicative of early ventricular fibrosis.²⁷ In addition to clinical cardiomyopathy, heart arrhythmias have been observed in cardiac tissue, and recent studies have shown connexin43 mislocalization as a contributor to disease pathology.²⁸ Connexin43 is a redox-sensitive gap junction protein which was found to be broken down when in the presence of MPO, due to indirect activation of matrix metalloproteinase 7.²⁹ In addition, MPO was found to induce fibroblast to myofibroblast trans-differentiation by activation of p38 mitogen-activated protein kinases which in turn will upregulate collagen within the tissue.²⁹ Connexin43 is especially important for the formation of heart structures such as the conotruncal region during cardiac development.³⁰ Past studies have shown that MPO is involved in regulating vascular tone within certain areas of the body. For instance, it was found that BF within the internal mammary artery and the left anterior descending artery, along with total myocardial perfusion, was decreased following MPO injections when compared against a control group ($p<0.001$)³¹. Likewise, our study has shown that there is a rapid decrease in blood flow following the 8-10 week time point, and a possible contributor may be associated with MPO signaling pathways as it was found to be significant ($p<0.03$) within cardiac tissue (Figure 2.9B, Figure 2.19).

Within the hind limb regions, there is an increase of 12.30% ($p=0.37$) in blood flow, 15.41% increase in blood volume ($p=0.26$), and a 3.89% increase in mean transit time ($p=0.87$) at the first time point of 4-5 weeks (Figures 2.9A, 2.10A, and 2.11A). At the later 8-10 week time point, there is a decrease by 3.45% in blood flow ($p=0.83$), an

increase by 10.62% in blood volume ($p=0.62$), and a 14.94% increase in mean transit time ($p=0.57$) (Figures 2.9B, 2.10B, and 2.11B). A past study completed by our lab indicated similar results with respect to blood volume in *mdx* mice, which was correlated with myofibrillar regeneration within skeletal muscle. Results also indicated that there was an increase in ^{18}F -FDG uptake within the tissue.³² Another study injected ^{133}Xe dissolved in isotonic saline into skeletal muscle and observed blood flow over 15 seconds. Clearance of the isotope was measured by using a collimated sodium iodide crystal scintillation detector which was coupled to a ratemeter with measurements taken every three seconds. Results indicated that mean blood flow to skeletal muscle was not significant despite the trends observed within the data. It was hypothesized that the significant difference might be obscured by the disease state of the tissue itself, with fatty deposits altering results³³. Thus, our research endeavor may shed light on why employing the use of imaging modalities is difficult in DMD.

		Brain	Heart	Hindlimbs/Skeletal Muscle
4-5 weeks	Blood Flow	↑	↑	↑
	Blood Volume	↑	↑	↑
	Mean Transit Time	↓	↓	↑
	MPO	↑	↑	No change
8-10 weeks	Blood Flow	↓	↑	↓

	Blood Volume	↓	↓	↑
	Mean Transit Time	↓	↓	↑
	MPO	↓	↑	↑

Table 2. Summary of qualitative changes within hemodynamic parameters (blood flow, blood volume, mean transit time) and MPO signal between the 4-5 week and 8-10 week time point.

2.5 Conclusions

Now that we have thoroughly analyzed the data, we must revisit our original hypothesis. We postulated that CT scans would model DMD progression by providing absolute quantification of perfusion. Thus, we have met the first hypothesis in our research investigation. Additionally, we hypothesized that oxidative stress might correlate with DCE-CT perfusion parameters to replicate the pathologic environment seen in later stages of DMD. As we will see in Chapter 3, results here do not indicate a clear answer, and this may be due to limitations within the study. On one hand, we had notable trends within the data, such as at the 4-5 week time point in the brain for blood flow and blood volume. However, extreme caution must be taken to not overinterpret the data as no values in DCE-CT hemodynamic parameters reached statistical significance.

In the discussion section, our findings in terms of MPO were supported by various investigations that came prior. We were able to use some of this groundwork to argue in instances that the role of oxidative stress influencing hemodynamic parameters may exist, given the trends seen in our data. Regardless, this study was one of the first to show body-wide CT perfusion in *mdx* mice and analyze the heart, brain, and skeletal muscle with respect to oxidative stress. Our findings are novel, and with the correct modifications to the study, I believe they will reach statistical significance. This, in turn,

would allow DCE-CT to have an excellent role in clinical diagnostic and DMD disease progression monitoring when other routes of diagnosis have been exhausted, given its low risk-to-benefit ratio.

2.6 References

1. Ortolan, P., Zanato, R., Coran, A., Beltrame, V. & Stramare, R. Role of radiologic imaging in genetic and acquired neuromuscular disorders. *Eur. J. Transl. Myol.* **25**, 121 (2015).
2. Shklyar, I. *et al.* Quantitative muscle ultrasound in Duchenne muscular dystrophy: A comparison of techniques. *Muscle and Nerve* **51**, 207–213 (2015).
3. Adorisio, R. *et al.* Duchenne Dilated Cardiomyopathy: Cardiac Management from Prevention to Advanced Cardiovascular Therapies. *J. Clin. Med.* **9**, 3186 (2020).
4. Power, A. *et al.* Echocardiographic Image Quality Deteriorates with Age in Children and Young Adults with Duchenne Muscular Dystrophy. *Front. Cardiovasc. Med.* **4**, (2017).
5. Schneider, S. M. *et al.* Glucose Metabolism as a Pre-clinical Biomarker for the Golden Retriever Model of Duchenne Muscular Dystrophy. *Mol. Imaging Biol.* **20**, 780–788 (2018).
6. Akin, E. A. & Washington, G. Optimizing Oncologic FDG-PET / CT Scans to Decrease Radiation Exposure. *Image Wisely Radiat. Saf. Adult Med. Imaging* 1–16 (2017).
7. Karim, H., Schmidt, B., Dart, D., Beluk, N. & Huppert, T. Functional near-infrared spectroscopy (fNIRS) of brain function during active balancing using a video game system. *Gait Posture* **35**, 367–372 (2012).
8. Weng, W.-C. *et al.* Cross-section and feasibility study on the non-invasive evaluation of muscle hemodynamic responses in Duchenne muscular dystrophy by using a near-infrared diffuse optical technique. *Biomed. Opt. Express* **9**, 4767 (2018).
9. Scarapicchia, V., Brown, C., Mayo, C. & Gawryluk, J. R. Functional magnetic resonance imaging and functional near-infrared spectroscopy: Insights from

- combined recording studies. *Front. Hum. Neurosci.* **11**, 1–12 (2017).
10. Iwatani, J. *et al.* Use of T1-weighted/T2-weighted magnetic resonance ratio images to elucidate changes in the schizophrenic brain. *Brain Behav.* **5**, 1–14 (2015).
 11. Vohra, R., Batra, A., Forbes, S. C., Vandenborne, K. & Walter, G. A. Magnetic Resonance Monitoring of Disease Progression in mdx Mice on Different Genetic Backgrounds. *Am. J. Pathol.* **187**, 2060–2070 (2017).
 12. Allmendinger, A. M., Tang, E. R., Lui, Y. W. & Spektor, V. Imaging of stroke: Part 1, perfusion CT - Overview of imaging technique, interpretation pearls, and common pitfalls. *Am. J. Roentgenol.* **198**, 52–62 (2012).
 13. Lehmann-Horn, F. *et al.* Rationale for treating oedema in Duchenne muscular dystrophy with eplerenone. *Acta Myol.* **31**, 31–39 (2012).
 14. O'Connor, J. P. B. *et al.* Dynamic contrast-enhanced imaging techniques: CT and MRI. *Br. J. Radiol.* **84**, (2011).
 15. Aranmolate, A., Tse, N. & Colognato, H. Myelination is delayed during postnatal brain development in the mdx mouse model of Duchenne muscular dystrophy. *BMC Neurosci.* **18**, 1–17 (2017).
 16. Xu, S. *et al.* Abnormalities in brain structure and biochemistry associated with mdx mice measured by in vivo MRI and high resolution localized 1H MRS. *Neuromuscul. Disord.* **25**, 764–772 (2015).
 17. Üllen, A. *et al.* Myeloperoxidase-Derived Oxidants Induce Blood-Brain Barrier Dysfunction In Vitro and In Vivo. *PLoS One* **8**, (2013).
 18. Florczyk-Soluch, U., Polak, K. & Dulak, J. The multifaceted view of heart problem in Duchenne muscular dystrophy. *Cell. Mol. Life Sci.* (2021) doi:10.1007/s00018-021-03862-2.

19. Cai, H., Chuang, C. Y., Hawkins, C. L. & Davies, M. J. Binding of myeloperoxidase to the extracellular matrix of smooth muscle cells and subsequent matrix modification. *Sci. Rep.* **10**, 1–13 (2020).
20. Pinniger, G. J., Terrill, J. R., Assan, E. B., Grounds, M. D. & Arthur, P. G. Pre-clinical evaluation of N-acetylcysteine reveals side effects in the mdx mouse model of Duchenne muscular dystrophy. *J. Physiol.* **595**, 7093–7107 (2017).
21. DeNichilo, M. O. *et al.* Peroxidase enzymes regulate collagen extracellular matrix biosynthesis. *Am. J. Pathol.* **185**, 1372–1384 (2015).
22. Kennedy, T. L. *et al.* Utrophin influences mitochondrial pathology and oxidative stress in dystrophic muscle. *Skelet. Muscle* **7**, 22 (2017).
23. Fainardi, E., *et al.* CT perfusion mapping of hemodynamic disturbances associated to acute spontaneous intracerebral hemorrhage. *Neuroradiology* **8**, 729-740 (2008).
24. Podkalicka, P., Mucha, O., Dulak, J. & Loboda, A. Targeting angiogenesis in Duchenne muscular dystrophy. *Cell. Mol. Life Sci.* **76**, 1507–1528 (2019).
25. Salam, E. A., Abdel-Meguid, I. E., Shatla, R. & Korraa, S. Evaluation of neural damage in Duchenne muscular dystrophy patients. *Acta Myol.* **33**, 13–18 (2014).
26. Doorenweerd, N. *et al.* Decreased cerebral perfusion in Duchenne muscular dystrophy patients. *Neuromuscul. Disord.* **27**, 29–37 (2017).
27. Meyers, T. A. & Townsend, D. Early right ventricular fibrosis and reduction in biventricular cardiac reserve in the dystrophin-deficient mdx heart. *Am. J. Physiol. - Hear. Circ. Physiol.* **308**, H303–H315 (2015).
28. Danik, S. B. *et al.* Modulation of cardiac gap junction expression and arrhythmic susceptibility. *Circ. Res.* **95**, 1035–1041 (2004).
29. Mollenhauer, M. *et al.* Myeloperoxidase Mediates Postischemic Arrhythmogenic

- Ventricular Remodeling. *Circ. Res.* **121**, 56–70 (2017).
30. Kotini, M. *et al.* Gap junction protein Connexin-43 is a direct transcriptional regulator of N-cadherin in vivo. *Nat. Commun.* **9**, (2018).
 31. Rudolph, T. K. *et al.* Myeloperoxidase deficiency preserves vasomotor function in humans. *Eur. Heart J.* **33**, 1625–1634 (2012).
 32. Ahmad, N. *et al.* Use of imaging biomarkers to assess perfusion and glucose metabolism in the skeletal muscle of dystrophic mice. *BMC Musculoskelet. Disord.* **12**, (2011).
 33. Paulson, O. B., Engel, A. G. & Gomez, M. R. Muscle blood flow in Duchenne type muscular dystrophy, limb-girdle dystrophy, polymyositis, and in normal controls. *J. Neurol. Neurosurg. Psychiatry* **37**, 685–690 (1974).
 34. Lee TY, Purdie TG, Stewart E. CT imaging of angiogenesis. *Q J Nucl Med.* 2003 Sep;**47**(3):171-87. PMID: 12897709.

Chapter 3

3 Conclusions and Future Directions

3.1 Study Summary

Immunofluorescence staining with MPO demonstrated statistically significant differences in the brain at the 4-5 week time point and 8-10 week time point in the heart and gastrocnemius tissue; MPO staining was notably higher than control groups in these cases. When analyzed in conjunction with H&E and Masson's trichrome data, it seems in some cases oxidative stress precede confirmation of fibrofatty deposits, infiltrate, and centric nuclei.

Furthermore, when results of histology for oxidative stress and pathogenesis are displayed and interpreted alongside DCE-CT perfusion parameters, some instances occur where one set of data may, in turn, validate or explain the findings of the other. However, it is important to note none of the DCE-CT perfusion parameters showed statistically significant differences. This was seen in cases of the brain, where trends indicated that an increase in blood flow and blood volume at the 4-5 week time point was noted to have increased MPO deposition, whereas, in the 8-10 week time point, a decrease in brain blood volume and blood flow was observed matching the decrease in MPO deposition. Similar trends such as the one mentioned prior with MPO and perfusion parameters also occurred in the myocardium for blood flow at both time points of 4-5 weeks and 8-10 weeks, where an increase in perfusion and an increase in MPO deposition was recorded.

3.2 Significance

This study raises other important questions, such as do sex differences influence hemodynamic parameters in relation to oxidative stress mechanisms and pathways? In addition, this study has laid the groundwork for future research pertaining to more severely affected animal models within DMD, such as double knockout and heterozygous mice. Thus, additional animal models should be used to validate and replicate this investigation. Further questions pertaining to how vasculature differs between these

dystrophins' knockout models and how to best model the disease in the human population must be explored.

The differing results in each area of the body have led us to believe in a survivorship hypothesis that certain areas of the body are protected and preserved at differing time points depending on use and function. This leads to existential questions pertaining to what came first, dysfunctional vasculature or reactive oxidative species within particular sites. If future studies successfully replicate our findings, the usage of DCE-CT may hold promise in the diagnosis and long-term monitoring of DMD patients. In addition, the use of DCE-CT could easily be integrated within clinical trials pertaining to therapeutics to track the changes body-wide for effectiveness and usefulness.

3.3 Limitations

With most imaging studies, there exist limitations within the realm of research conducted. Some limitations include that CT scans were analyzed and computed using software requiring manual ROI segmentation was used to encompass areas of the heart, brain, and hind limb muscle.¹ While ROI area was kept relatively constant, user bias cannot be discounted as pixel size and visual acuity are limiting factors when creating masks to determine ROI coverage and excluded sections.² Another caveat of DCE-CT lies in the spatial resolution achieved when performing small animal imaging.³

Further, both the samples used for the IHC cohort, and the DCE-CT cohort were not analyzed for sex differences given low sample size due to extenuating circumstances and time constraints. Sex differences have been cited to significantly alter reactive oxidant species levels within cardiovascular disease; however, the specific cause is unknown.⁴ Recent studies have speculated that this occurrence may be due to the difference between signaling pathways involved in the production and deactivation of reactive oxygen metabolites.⁵ Consequently, the effect of sex-based differences within inflammatory pathways is also unknown with respect to its body-wide effects. Males are often associated with higher levels of inflammatory and reactive oxidant species levels prior to puberty, whereas in later stages of life, females are predicted to have elevated levels of both inflammatory and ROS markers. More specifically, the differing effect of

testosterone and estrogen on the mitochondria with respect to oxidative stress has proven significant; as estrogen is often noted to be involved in protective pathways combating ROS.^{6,7}

Despite the *mdx* mouse model being one of the most characterized and used DMD mouse models, it does have limited use pertaining to the clinical effects seen in DMD patients. Although the *mdx* mouse lacks dystrophin expression and has similar disease pathology as seen in humans, it does not have an equally reduced lifespan or the exact severity of DCM, nor do symptoms appear along similar timelines with respect to disease progression.⁸

3.4 Future Directions

Given the results of oxidative stress using MPO as a biomarker, additional experiments should be conducted with respect to its endogenous RNA level. Specifically, following CT scans, tissue collected from mice should be used to quantify RNA expression on specific oxidative stress genes using a PCR array. In doing so, the correlative effect of mean transit time, blood volume, or even blood flow can be analyzed for transcription levels within cardiac, brain, and hindlimb tissue at the pre-fibrotic and fibrotic time points.

Given the limitations associated with the *mdx* mouse model, future work should include additional DMD genotypes, such as the DKO mouse model and the heterozygous mouse model. Utilizing these murine models will characterize the differing effects of dystrophin null and utrophin null mice and shed better light on our recent results with the *mdx* mouse model. The impact of utrophin on hemodynamic parameters and oxidative stress, in general, remains unknown. Therefore, the sample size should be increased at both time points with a minimum of six biological replicates to account for individual differences amongst species while boosting the internal and external validity of the study. In addition, as noted above, sex differences are apparent in oxidative stress pathways. Given that the cause is unknown, it is best to characterize these differences further in DMD animal models.

Lastly, injection of Conray 50 dye occurred via tail vein catheter using a pump. Given the etiology of the disease, dye uptake can be influenced by the leakiness of the vasculature. Publications have stated that vasculature is impaired in DMD patients. As such, the leakiness of the blood-brain barrier must be considered and can be calculated using additional DCE-CT maps to assist with troubleshooting any discrepancies in perfusion.⁹

3.5 Conclusion

Now that we have thoroughly analyzed the data, we must revisit our original hypothesis. We postulated that CT scans would model DMD progression by providing absolute quantification of perfusion. Thus, we have met the first hypothesis in our research investigation. Additionally, we hypothesized that oxidative stress might correlate with DCE-CT perfusion parameters to replicate the pathologic environment seen in later stages of DMD. Results observed in Chapter 2 do not indicate a clear answer, and this may be due to limitations within the study. On one hand, we had notable trends within the data, such as at the 4-5 week time point in the brain for blood flow and blood volume. However, extreme caution must be taken to not overinterpret the data as no values in DCE-CT hemodynamic parameters reached statistical significance.

In the discussion section, our findings in terms of MPO were supported by various investigations that came prior. We were able to use some of this groundwork to argue in instances that the role of oxidative stress influencing hemodynamic parameters may exist, given the trends seen in our data. Regardless, this study was one of the first to show body-wide CT perfusion in *mdx* mice and analyze the heart, brain, and skeletal muscle with respect to oxidative stress. Our findings are novel, and with the correct modifications to the study, I believe they will reach statistical significance. This, in turn, would allow DCE-CT to have an excellent role in clinical diagnostic and DMD disease progression monitoring when other routes of diagnosis have been exhausted, given its low risk-to-benefit ratio.

Without additional modifications to the study, such as increased sample size and segregation by sex differences, the data reported in this study cannot be interpreted with absolute certainty. Despite this unfortunate caveat, our group is still confident that data

will likely reach statistical significance once these alterations are included. As the study currently stands, this research has shed light on one possible oxidative stress pathway to explain changes in hemodynamic parameters within three different areas of the body, thus rendering a snapshot of the body-wide affects in DMD.

3.6 References

1. Jensen, N. K. G. *et al.* Prediction and Reduction of Motion Artifacts in Free-Breathing Dynamic Contrast-Enhanced CT Perfusion Imaging of Primary and Metastatic Intrahepatic Tumors. *Acad. Radiol.* **20**, 414–422 (2013).
2. Courtier, J. L. & Glastonbury, C. M. Bias in Radiology : The How and Why of Misses and. 236–247 (2018).
3. Cicalini, E. *et al.* A high spatial resolution CT scanner for small animal imaging. *Nucl. Phys. B - Proc. Suppl.* **150**, 313–316 (2006).
4. Tenkorang, M. A., Snyder, B. & Cunningham, R. L. Sex-related differences in oxidative stress and neurodegeneration. *Steroids* **133**, 21–27 (2018).
5. Kander, M. C., Cui, Y. & Liu, Z. Gender difference in oxidative stress: a new look at the mechanisms for cardiovascular diseases. *J. Cell. Mol. Med.* **21**, 1024–1032 (2017).
6. Liao, T. L. *et al.* Mitochondrial translocation of estrogen receptor β affords resistance to oxidative insult-induced apoptosis and contributes to the pathogenesis of endometriosis. *Free Radic. Biol. Med.* **134**, 359–373 (2019).
7. Razmara, A., Duckles, S. P., Krause, D. N. & Procaccio, V. Estrogen suppresses brain mitochondrial oxidative stress in female and male rats. *Brain Res.* **1176**, 71–81 (2007).
8. Yucel, N., Chang, A. C., Day, J. W., Rosenthal, N. & Blau, H. M. Humanizing the mdx mouse model of DMD: the long and the short of it. *npj Regen. Med.* **3**, (2018).
9. Fainardi, E., *et al.* CT perfusion mapping of hemodynamic disturbances associated to acute spontaneous intracerebral hemorrhage. *Neuroradiology* **8**, 729-740 (2008).

Appendices

Appendix A: Approval of Animal Protocols



2017-038:9:

AUP Number: 2017-038
AUP Title: Hoffman Breeding Protocol
Yearly Renewal Date: 05/01/2021

The YEARLY RENEWAL to Animal Use Protocol (AUP) 2017-038 has been approved by the Animal Care Committee (ACC), and will be approved through to the above review date.

Please at this time review your AUP with your research team to ensure full understanding by everyone listed within this AUP.



AUP Number: 2018-140
PI Name: Hoffman, Lisa M
AUP Title: Non-Invasive Imaging of Therapeutics in Mouse Models of DMD
Approval Date: 07/01/2019

Official Notice of Animal Care Committee (ACC) Approval:

Your new Animal Use Protocol (AUP) 2018-140:1: entitled " Non-Invasive Imaging of Therapeutics in Mouse Models of DMD"

has been APPROVED by the Animal Care Committee of the University Council on Animal Care. This approval, although valid for up to four years, is subject to annual Protocol Renewal.

Prior to commencing animal work, please review your AUP with your research team to ensure full understanding by everyone listed within this AUP.

Curriculum Vitae

Name: Sarah Hakim

Post-secondary Education and Degrees

M.Sc. Medical Biophysics candidate (2019-present)

Supervisors: Dr. Lisa Hoffman

Thesis: Modelling systemic oxidative stress within Duchenne Muscular Dystrophy using CT perfusion

Western University

Schulich School of Medicine & Dentistry, London, Canada

BMSc Honours Specialization in Interdisciplinary Medical Sciences (2015-2019)

University of Western Ontario, London, Canada

Honours and Awards

- | | |
|-----------------|---|
| 2020/5 – 2021/5 | CIHR CGSM - Fredrick Banting and Charles Best Canada Graduate Scholarship |
| 2020/9 | Women in Molecular Imaging Network Scholar Award - World Molecular Imaging Society |
| 2019/9 – 2021/8 | Western Graduate Research Scholarship |
| 2019/5 | Interdisciplinary initiative in Stem Cells and Regenerative Medicine summer studentship University of Western Ontario |

Related Work Experience

- | | |
|---------------------|---|
| (2021/1 – Present) | Resource Officer Schulich EDI Committee, Schulich School of Medicine and Dentistry - Equity Diversity Inclusion Council |
| (2020/10 – Present) | MBP Graduate Student Representative Schulich EDI Committee, University of Western Ontario |
| (2019/11 – Present) | Participant/Membership, Molecular Imaging Journal Club |
| (2020/6 – 2021/6) | Medical Biophysics Graduate Student Association - Academic Representative, University of Western Ontario |
| (2020/6 – 2021/6) | Medical Biophysics Graduate Student Association - St. Joseph Hospital Representative, University of Western Ontario |
| (2019/5 – 2019/8) | Student Research Assistant
Medical Biophysics, University of Western Ontario, Lawson Health Research Institute |
| (2018/9-2019/4) | Work-Study Student
Medical Biophysics, University of Western Ontario, University of Western Ontario |

PRESENTATIONS

1. (2021). Modeling Ischemia Body-Wide Duchenne Muscular Dystrophy. Children's Health Research Day, London, Canada
2. (2020). Non-invasively modeling ischemia in Duchenne Muscular Dystrophy. World Molecular Imaging Congress, Prague, Czech Republic
3. (2020). Modeling ischemia in Duchenne muscular dystrophy. Canadian Bone and Joint Conference, Canada
4. (2019). Modeling body-wide inflammation in Duchenne Muscular Dystrophy. Lawson Summer Student Symposium, Canada
5. (2019). The non-invasive modeling of body-wide inflammation in Duchenne muscular dystrophy. Canadian Connective Tissue Conference, Canada

PUBLICATIONS

Conference Publications:

Sarah Hakim, Lise Desjardins, Jennifer Hadway, Dr. Lisa Hoffman. (2021). Modeling Oxidative Stress in Duchenne Muscular Dystrophy. Conference Program. London Health Research Day Conference Date: 2021/5

Hakim, S., Desjardins, L., Hadway, J., McClennan, A., Hoffman, L.M. (2020). Non-invasively modeling ischemia in Duchenne Muscular Dystrophy. Conference Program. World Molecular Imaging Congress Conference Date: 2020/10

Hakim, S., Desjardins, L., Hadway, J., McClennan, A., Hoffman, L.M. (2020). Modeling ischemia in Duchenne muscular dystrophy. Conference Program. Canadian Bone and Joint Conference Date: 2020/6

Tang, J.M., McClennan, A.J, Hakim, S., Hadway, J., Smailovic, H., Fox, M., Anazodo, U.C., Hoffman, L.M. (2019). *Non-invasive modeling of body-wide Inflammation in Duchenne Muscular Dystrophy in-vivo animal models*. Conference Program. World Molecular Imaging Congress
Conference Date: 2019/8

Hakim, S., Shweiki Y.A., Naghibosadat, M., McClennan, A.J., Luyt, L., Dhanvantari, S., Hoffman, L.M. (2019). Ghrelin Receptor Binding in Cardiac Tissue is Altered with Cardiovascular Inflammation in Duchenne Muscular Dystrophy. Conference Program/Agenda. Canadian Connective Tissue Conference Date: 2019/5

Kashyap, N., M. Ahmed, S. Hakim, Y. Shweiki, A. McClennan, and L. Hoffman. (2019). Investigating CCN family proteins as a potential therapeutic target in Duchenne Muscular dystrophy. Program Agenda. Child Health Research Day
Conference Date: 2019/4

